An exact Relation of the constant and periodical winds…
is a part of Natural History no less desirable and useful,
than it is difficult to obtain, and its
Phenomena hard to explicate

Halley, 1686

Chapter 4

Mass and Wind Fields

Overview: Radiative balance showed there must be winds to transport heat. Temperature variations create pressure patterns. Pressure is a force initiating and sustaining the winds. Thus, the pressure and wind patterns are intertwined. Mass and motion can be broadly explained using simple models, including models that connect back to build further understanding of the heat transport.

4.1 Mass Fields

4.1.1 Geopotential Height Fields Overview

The hypsometric equation (C.13) shows that the spacing between isobaric surfaces is proportional to the temperature of the air between those surfaces. Figure 4.1 shows that the zonal and seasonal average 1000 hPa heights, Z_{1000} (i.e. near sea level) have small variation compared to the variation of higher elevation pressure surfaces. Hence, the warmer tropics have much higher geopotential heights at 500 hPa (Z_{500}; Figure 4.1a) than do colder higher latitudes. Though high, the middle and upper troposphere geopotential heights are relatively flat in the tropics, as anticipated from the similarly weak horizontal temperature gradient there (Figure 3.20). The horizontal gradients of temperature and height are both larger in middle latitudes. This gradient has an obvious seasonal shift with most of the gradient located from ~20-60 degrees latitude in winter and higher latitudes in summer. The midtropospheric pressure surface heights are lower in polar regions and lowest during winter. Thus the midlatitude Z_{500} gradient is strongest in winter in both hemispheres. The seasonal shift in the latitude range of the gradient and the change in gradient magnitude are both larger in the Northern Hemisphere. Troughs in Z_{1000} are found near the equator and in middle latitudes; between is relatively higher pressure in the subtropics.

Several other general comments about Figure 4.1 are as follows.

1) As anticipated in §1.2, the meridional gradient of pressure in the troposphere increases with height.
2) Generally, the 1000hPa height has less meridional variation than isobaric surfaces for lower pressures. The 100 hPa height field has similar shape to the 500 hPa field shown but the amplitude is approximately twice as large (Grotjahn, 1993; Fig. 3.21).
3) The meridional pressure gradient at high altitudes is less in summer due to strong solar heating that is rather uniform with latitude (Figure 3.6).
4) The hemispheric average surface pressure is less in the summer and greater in the winter in both hemispheres. This indicates a net shift of mass between the two hemispheres.
5) The difference between the hemispheres is largely removed as one goes to higher altitudes; it is almost gone by 100 hPa.
6) The Z_{1000} equatorial trough combined with the subtropical highs creates a low level pressure gradient force that is opposite to the pressure gradient visible for Z_{500}. These gradients are consistent with Hadley circulations.
7) The Z_{1000} tropical trough (later located with moist convection) moves seasonally into the summer hemisphere. Thus the Z_{1000} pattern is consistent with the Hadley cell being stronger in the winter hemisphere and expanding across the equator.
8) Low pressure lies at the extratropical cyclone “storm tracks”.

4.1.2 Midlatitude Planetary Waves and Storm Tracks

As discussed in Chapter 1, the midlatitude weather is dominated by traveling frontal cyclones, also known as extratropical cyclones. The time mean Z_{500} fields (Figures 4.2 and 4.3) show that the mid and upper tropospheric pressure pattern has long waves, especially in the Northern Hemisphere.

Also called ‘planetary waves,’ the long wave pattern in the mass fields can be anticipated from the mid tropospheric temperature (T_{700}) pattern shown in Chapter 3 (Figure 3.24) and hypsometric balance. The Northern Hemisphere has main troughs near the east coasts of North America and Asia that are associated with the cold air over Canada/Greenland and eastern Siberia. The Asian east coast upper-level trough is not present during summer, but the eastern North American trough remains. Presumably, the melting of the snow cover over Siberia allows that region to warm up enough during summer. But, the Greenland and Baffin Island ice sheets

inhibit this process (thus acting rather like Antarctica in the opposite hemisphere). A weaker trough extends over the Mediterranean and Northwest Africa during DJF. Ridges are found in between, most prominently in northwestern North America and Europe. In contrast, the time average Southern Hemisphere height pattern tends to be rather zonal with one deep low centered over very cold Antarctica. Southern Hemisphere time average troughs are harder to see and are barely visible in each of the three ocean basins at 50S.

Both the Z_{500} and T_{700} fields have troughs near the east coasts of North America and Asia during winter. Close inspection shows that the T_{700} trough is slightly west of the Z_{500} trough. The colder temperatures at lower levels (Figure 3.23) are also over those continents but while the 1000-500hPa thickness is less there, the sea level pressure (SLP; Figure 4.4) is higher there.

Close inspection finds time mean SLP troughs to be slightly east of the Z500 troughs. These orientations of the thermal and pressure troughs support frontal cyclogenesis. The thermal trough upstream of the geopotential trough creates an 'upstream tilt' of the trough axis with increasing elevation. How this offset of temperature and mass can amplify the mid-tropospheric geopotential trough can be shown several ways. One way is with the so-called baroclinic equivalent barotropic vorticity equation (or BEBVE).

The BEBVE is a variant on the vertical component vorticity equation. Cartesian geometry is sufficient to show how the thermal trough being upstream of the geopotential trough promotes growth of the pressure trough. The derivation is as follows (after Carlson, 1991). Consider the quasi-geostrophic vorticity equation

$$\frac{\partial \zeta}{\partial t} + V_g \bullet \nabla \{\zeta + f\} = f \frac{\partial \omega}{\partial p} \tag{4.1}$$

Partition the geostrophic wind into two parts:

$$\boldsymbol{V}_g = \boldsymbol{V}_{gm} + B(p)\boldsymbol{V}_{Th} \tag{4.2}$$

Parameter B contains all the variation of $\boldsymbol{V_g}$ with pressure. Since $\boldsymbol{V_{gm}}$ is the vertical average geostrophic wind, then $B=0$ at the level where the geostrophic wind ($\boldsymbol{V_g}$) equals $\boldsymbol{V_{gm}}$ and the vertical (pressure) average of B is zero. This level is near 500 hPa. Thus $\boldsymbol{V_{gm}}$ and associated vertical average geostrophic vertical component of vorticity, ζ_{gm} are defined as:

$$\begin{aligned} \boldsymbol{V}_{gm} &= \frac{1}{p_s}\int_0^{p_s} \boldsymbol{V}_g \, dp = \frac{g}{f_0 \, p_s}\int_0^{p_s} \vec{k} \times \vec{\nabla} Z \, dp \\ \zeta_{gm} &= \boldsymbol{k} \bullet \nabla \times \boldsymbol{V}_{gm} \end{aligned} \tag{4.3}$$

The $\boldsymbol{V_{Th}}$ wind component is a variation on the 'thermal wind' (shear) concept in being calculated from the vertical average thickness field (*Th*). This geostrophic wind $\boldsymbol{V_g}$ can have turning when the directions of $\boldsymbol{V_{Th}}$ and $\boldsymbol{V_{gm}}$ differ. They differ when the thermal field is offset from the mass field. Turning indicates temperature advection, but the turning is simplified by the separation of variables placing all the vertical variation of $\boldsymbol{V_{Th}}$ in *B(p)*. This 'thermal wind' has an associated 'thermal vorticity'. Their definitions are:

$$\begin{aligned} \boldsymbol{V_{Th}} &= \frac{g}{f_0\, p_s} \int_0^{p_s} \boldsymbol{k} \times \nabla Th \\ \zeta_{Th} &= \boldsymbol{k} \bullet \nabla \times B(p) \boldsymbol{V_{Th}} \end{aligned} \tag{4.4}$$

Therefore

$$\zeta = \zeta_{gm} + \zeta_{Th} \tag{4.5}$$

The equivalent barotropic vorticity equation is derived by substituting (4.2) and (4.5) into (4.1) and integrating over the range of pressure.

$$\begin{aligned} &\frac{1}{p_s} \int_0^{p_s} \frac{\partial \zeta}{\partial t} dp + \frac{1}{p_s} \int_0^{p_s} \boldsymbol{V_g} \bullet \nabla \left\{ \zeta + f \right\} dp = \frac{f}{p_s} \int_0^{p_s} \frac{\partial \omega}{\partial p} dp \\ &\frac{1}{p_s} \int_0^{p_s} \left\{ \frac{\partial \zeta_g}{\partial t} + B \frac{\partial \zeta_{Th}}{\partial t} \right\} dp + \frac{1}{p_s} \int_0^{p_s} \left\{ \boldsymbol{V_{gm}} + B \boldsymbol{V_{Th}} \right\} \bullet \nabla \left\{ \zeta_{gm} + B \zeta_{Th} + f \right\} dp = \frac{f}{p_s} \left\{ \omega_{sfc} \right\} \end{aligned} \tag{4.6}$$

Where ω_{sfc} is the pressure velocity at $p=p_s$. The nonlinear terms do not have 'cross' products of thermal and geostrophic components because the vertical integral of *B* vanishes. However the vertical integral of B^2 will not vanish. Simplifying obtains the BEBVE:

$$\frac{\partial \zeta_{gm}}{\partial t} = -\boldsymbol{V_{gm}} \bullet \nabla \left\{ \zeta_{gm} + f \right\} - \boldsymbol{V_{Th}} \bullet \nabla \zeta_{Th} \frac{1}{p_s} \int_0^{p_s} B^2 \, dp + \frac{f}{p_s} \left\{ \omega_{sfc} \right\} \tag{4.7}$$

The B^2 term is the key for the growth of the geostrophic vorticity and by extension growth of the vertical mean geopotential trough. If the thermal trough is upstream from the geopotential trough, then the B^2 term will be positive where ζ_{gm} is positive thereby amplifying ζ_{gm} and thus the geopotential trough at 500 hPa.

At the base (equatorward side) of each trough the height contours are more closely spaced; from geostrophic wind balance one expects the wind speeds to be relatively stronger there. Consistent with the zonal average distribution (Figure 4.1) the time average Z_{500} gradient (Figure 4.2) is strongest in middle latitudes. While the peak gradient (the slope in figure 4.1a) is similar all year in the Southern Hemisphere, the net change from equator to pole is smaller in the

summer. In the Northern Hemisphere the net change and the gradient are both weaker during summer.

Frontal cyclones form, propagate, and decay in specific regions. Figure 4.2 shows various archetypal tracks followed by many frontal cyclones. The tracks are a schematic synthesis of material presented in these sources: van Loon (1966), Whitaker and Horn (1984) ,Simmonds and Murray (1999), Hoskins and Hodges (2002), Hoskins and Hodges (2005), and Dos Santos Mesquita (2008). Individual tracks of cyclones vary, but the thicker dashed arrows indicate schematically the more common paths.

Cyclogenesis is favored in three types of regions: i) near the east coasts of continents, ii) where large-scale surface temperature gradients are strong, and iii) on the lee side of major mountain ranges. The long wave troughs near those east coasts have stronger height gradient and therefore stronger geostrophic winds. From simple baroclinic instability arguments, perturbations on the flow can amplify more rapidly where the vertical shear is larger (1.5). As discussed in Chapter 1, there are qualifiers such as the latitude and static stability. Consistent with thermal wind shear, the stronger winds lie above stronger temperature gradients so one can base the baroclinic instability argument on either the vertical shear or the horizontal temperature gradient. The time mean surface temperature gradient is also strong near the east coasts of North America and Asia due to the juxtaposition of cold land mass and oceanic WBCs. A region of stronger meridional sea surface temperature gradient lies south of Africa and across much of the Southern Indian Ocean. Further south, the near-surface temperature gradient is intensified at the edge of Antarctic sea ice. Finally, simple potential vorticity arguments can explain cyclogenesis preference downwind of mountain ranges with meridional extent.

The Ertel potential vorticity (Q_E) is a conserved quantity for adiabatic motion in potential temperature coordinates (Appendix C.3); from (C.49):

$$Q_E = g\frac{\zeta_g + f}{\frac{\partial p}{\partial \theta}} \tag{4.8}$$

In middle latitudes the flow is generally westerly. Imagining a westerly flow encountering the mountain ranges of the western North America, such a straight flow has no curvature vorticity where it first encounters the mountains. Ascending the mountains the spacing (i.e. ∂p) between θ surfaces decreases thereby reducing the denominator in (4.8). To maintain a constant Q_E the numerator must also decrease, by developing some anticyclonic vorticity. The flow develops an equatorward component and as the latitude changes f decreases as well. As air crosses the ridge line it descends on the lee side, so the θ surfaces spread apart again and the denominator

increases. The absolute vorticity must increase to match, but the air is at a lower latitude than before encountering the mountains and must have positive relative vorticity to conserve Q_E. Expressed as curvature, the positive vorticity eventually turns the flow poleward. This motion and vorticity imply a geopotential height trough. It is this trough that can be a 'seed' for cyclone formation.

Frontal cyclones generally progress eastward and poleward as they evolve. These cyclones often merge with or supplant the 'semi-permanent' Aleutian and Icelandic lows that are visible in the SLP field of Figure 4.4. The storm tracks show up in the precipitation fields (Chapter 5) as bands of heavier precipitation across the oceans in middle latitudes. Precipitation also is enhanced where these storm tracks encounter mountain ranges of northwestern North America, the southern Andes, and Western Europe.

Close inspection of Figure 4.2 shows the Northern Hemisphere storm tracks tend to lie just east (downstream) of the time average troughs. The analysis above provides a simple explanation to maintain the time average Z_{500} troughs. To understand the extratropical storm track location requires a few more concepts. First, the baroclinic instability theory (of Chapter 1) finds greater instability where the wind shear is greater. One may estimate the vertical wind shear from gradient winds and by assuming the time average flow is much stronger at 500hPa than near the surface. The southeastern sides of these troughs have the greater vertical shear and thus more baroclinic instability. Second, it takes time for frontal cyclones to grow to appreciable size by this mechanism and they are swept downstream as they grow. Third, as will be shown later, these baroclinic eddies grow by transporting heat from warmer to colder regions and *vice versa*. This transport occurs by warm advection 'ahead' and cold air advection 'behind' of the lower troposphere trough. Since the time mean Z_{500} trough is created by the time mean cold air through the troposphere, the favorable position for the eddy to have cold air advection is downstream of the cold air. Indeed, the cyclogenesis *develops* upstream tilt of the trough axis in the vertical (Grotjahn and Tribbia, 1995; Grotjahn, 1996). This tilt is evident when comparing the troughs near the east coasts of North America and Asia in Figures 4.2 and 4.4. The SLP trough is east of the Z_{500} trough in both places. Similarly, ahead of the lower troposphere trough, the warm air advection builds thickness and thus builds an upper level ridge in Z_{500}. Classic works link surface cyclogenesis to upper level positive vorticity advection (e.g. Sutcliffe, 1947) and or temperature advection (e.g. Petterssen, 1956).

Figures like 4.2 are static images of the time mean patterns, however weather systems travel and the pressure pattern oscillates. The storm tracks like those in Figure 4.2 can be

obtained several ways and tend to fall into two groups: direct techniques that track individual centers and proxy techniques that track frontal cyclone quantities. Proxy techniques include band pass time filtering of height or meridional wind (e.g. Hoskins et al., 1989; Blackmon et al., 1977), tracking deviations from a zonal average, and energetic quantities (e.g. Cai et al., 2006, review). Direct tracking pressure centers (e.g. Whitaker and Horn, 1984), tracking Laplacian of SLP centers (e.g. Simmonds and Murray,1999; Sinclair, 1997), and using closed contours (Wernli and Schwierz, 2006). These techniques vary in complexity and have different advantages and disadvantages. For example, vorticity is a better estimator of cyclone strength since large pressure falls may arise mainly by the system tracking over a region of generally lower pressures (e.g. Sanders and Gyakum, 1980). However, vorticity tends to be very 'noisy' with multiple centers associated with a single low pressure center. The storm tracks have fascinating details (such as the midwinter suppression of the North Pacific storm track, e.g. Nakamura et al., 2004) mainly collected in Chapter 10. Reviews include Chang et al. (2002) and Shaw et al. (2016).

An easily calculated indirect storm track metric, square root of the time variance geopotential $\overline{RMS\left(Z^{''}\right)}$ is shaded in Figure 4.3. Several of the metrics listed here, including that in Figure 4.3, have the drawback of emphasizing the later stages in the frontal cyclone life-cycle because they are proportional to the amplitude of the storm and missing the early, small amplitude period of cyclone development. Hence, maximum values are located downstream from the long wave troughs.

Four general features are seen the zonal average time variances of Figure 4.3b,d. This figure uses more recent reanalysis data to update a similar figure by van Loon (1973, reproduced in Grotjahn, 1993).

1) The variability is greater in midlatitudes than in the tropics. The pressure variations are small in the tropics on the time mean (Figure 4.2) as is the variance (Figures 4.3b,d) because the temperature variations are small there. The $\left[RMS\left(Z^{''}_{1000}\right)\right]$ has similar variation as SLP variance; the increase of sea level pressure variance with latitude has been known for a long time; van Loon cites Lockyer (1910) and Köppen (1882).
2) The activity is highest during winter, but the seasonal change of the peak values is generally smaller in the Southern Hemisphere. The frontal cyclones gain much of their energy from baroclinic energy conversions that are proportional to the

horizontal temperature gradient. The horizontal temperature gradient decreases more from winter to summer in the Northern Hemisphere than in the Southern Hemisphere (recall Figure 3.22).

3) The maximum values of variance are centered near 62N and 58S during winter. These locations are poleward of the locations in van Loon. These locations fit the characteristic of frontal cyclones progressing eastward and poleward. At the storm track end, “cut-off” lows are sometimes developed and sometimes the tracks merge with these deep lows. In the Northern Hemisphere, the tracks often terminate near the Aleutian and Iceland islands leading to the maximum variance between 50 to 60N. In the Southern Hemisphere there are maxima near 50 to 60S. These data do not show another maximum van Loon found near 75°S.
4) The larger values of variance are spread out more broadly in latitude in the Northern Hemisphere. The greater spread reflects the greater meandering of the storms as they follow the persistent long wave pattern. In contrast, the Southern Hemisphere storms tend to track along a latitude circle more closely, especially during summer (Figure 4.2b).

4.1.3 Sea Level Pressure, Subtropical Highs, and Hadley Cells

Near surface pressure maps showing much of the globe were produced in the late 1800’s (e.g., Buchan, 1889). Figure 4.4 shows the global sea level pressure pattern during seasons of 3-month length. The equatorial trough is weak and quite longitudinally variable. In the subtropics, the lowest pressures are over land areas during the summer. SLP over southern Asia during JJA is especially low. The time-mean pattern over subtropical oceans is dominated by large anticyclonic gyres. In midlatitudes the pressure is relatively higher or lower between ocean and continent, depending on season. Some areas have persistent low pressure, the main example being off the Antarctic coastline.

Figure 4.4 shows a striking reversal of the near-surface pressure pattern from winter to summer in the Northern Hemisphere. During winter there are deep lows centered over the north Atlantic and north Pacific (the Icelandic and Aleutian lows) with high pressure over the continents (the Siberian and Canadian highs). The Northern Hemisphere subtropical highs are comparatively weak during winter. The summer pattern is the reverse of this; the subtropical highs have expanded in area over the oceans and the pressure is lower over the land. The Aleutian low has all but disappeared (in the summertime mean), while the Icelandic low has

shrunk and is centered over Baffin Island. The pressure pattern over the land can be explained as a surface thermal effect. Pressure at any level is the weight of the air above that point. In winter the cold surface air is denser; in summer the warm air is less dense compared to the nearby ocean. The hypsometric equation also makes that colder air less thick than warmer air so the cold high is shallow. Similar reasoning explains how the hot low is also shallow. The shallowness is evident by comparison to Figure 4.3. The opposite pressure pattern prevails in the mid and upper troposphere.

The Southern Hemisphere SLP pattern is different. The subtropical highs tend to be centered over the oceans all year. The midlatitude pattern is clearly much more zonal *on a time average*, with a belt of intense low-pressure cells centered near the coast of Antarctica. The pattern explains the very low Z_{1000} heights remarked upon earlier (Figure 4.1). Little seasonal change is apparent except over the continents.

A Chapter 1 ‘thought problem’ concluded that the Hadley cell was a reasonable approximation to the zonal average circulation of the tropics. Chapter 3 temperature patterns revealed that the Hadley cell of the winter hemisphere is stronger than of the summer hemisphere. Geostrophic wind balance breaks down in the boundary layer and near the equator. Thus the pressure gradient accelerates the winds ageostrophically, and recalling Ekman balance (§1.4.2) the motion has a component from higher to lower pressure from these subtropical highs. Synthesizing this information, it is immediately apparent that the equatorial sides of the subtropical highs generate equatorward flow consistent with the low-level branch of each Hadley cell (Figure 4.5). What is less apparent is why the Northern Hemisphere subtropical highs are stronger in *summer* when the Hadley cell is stronger in *winter*. Close inspection of Figures 4.4 or 4.5 resolves this seeming contradiction. The strength of the subtropical high as measured by the peak central pressure is not an infallible indicator of the meridional gradient from that high in the deep tropics. To wit: around 10N, the SLP gradient and meridional component of the near-surface winds is stronger in DJF than in JJA in the Indian, western and central Pacific, and Atlantic oceans as well as Africa (Figure 4.5). The two Northern Hemisphere subtropical highs are stronger in summer (over the oceans) because there is less frontal cyclone intensity in the oceanic storm tracks. The frontal cyclones suppress the subtropical highs over a seasonal average. However, the winter continental high in central Asia is much stronger than any subtropical high during summer, consistent with the stronger Hadley cell. Specifically, one might argue this consistency from Figure 4.5 at longitudes 100E-120E.

In the Southern Hemisphere, the conundrum largely vanishes. Southern Hemisphere subtropical highs have quite different seasonal change than the Northern Hemisphere (Grotjahn, 2004; Grotjahn and Osman, 2007). The Indian and South Atlantic subtropical highs are strongest during winter (JJA) while the South Pacific subtropical high is strongest during spring. Figure 4.5 around 10S shows the stronger SLP gradient and equatorward winds during winter over the Atlantic Ocean and the Indian Ocean across most of the Pacific.

The midlatitude, *zonal average* troughs result from preferred tracks by frontal cyclones. A prominent difference between hemispheres is the Southern Hemisphere zonal average trough is much deeper than in the Northern Hemisphere. This difference arises from the different amounts of land masses shown in Figure 1.2 and the orientation of the frontal cyclone storm tracks seen in Figure 4.2. The land mass differences are evident in Figure 4.4. The continental regions tend to have higher sea level pressure in winter and the oceans lower pressure. Therefore, when averaging around a latitude circle there are regions of high and low pressure that partly compensate in the Northern Hemisphere. In contrast, between 40 S and 70 S one finds SLP contours nearly parallel to latitude circles *on a time average*. Further south, hugging the Antarctic coast is chain of low pressure centers in Figure 4.4; thus, the zonal mean pressure is very low. This minimum has been discussed before (e.g., van Loon and Shea, 1988).

The distribution of Z_{1000} in the tropics and subtropics can be explained by general physical arguments. A set of simple arguments, paralleling those in Grotjahn (1993), provide a starting place, but to understand the circulation requires additional development.

To begin, one might imagine a horizontally uniform atmosphere from 30S to 30N. The temperature surfaces are ‘flat’ but the temperature profile is conditionally stable, meaning the lapse rate lies between the moist (saturated) and dry (unsaturated) rates. Initially, there is no moist convection. Imagine moist convection introduced near the equator, where a Hadley circulation has upward motion. The rising air within those clouds releases latent heat that reduces the cooling by adiabatic ascent enough so that the air where the convection occurs is warmer. Technically, the latent heating increases the potential temperature of the air that feeds into local sinking adjacent to those clouds where it is expressed as higher temperatures. In this way, the latent heating warms the tropical atmosphere indirectly (Randall, 2015; p.172). From the hypsometric relation, this warmer air causes high pressure aloft compared with the subtropics, setting up an equatorward pressure gradient in the upper troposphere. This gradient would drive ageostrophic motion poleward that could shift mass from the equatorial to the subtropical regions. Since the pressure at an elevation is the weight of all the air above, the pressure in the

lower troposphere would become higher in the subtropics and lower below the equatorial convection. Hence, a pressure gradient in the lower troposphere is set up that forces ageostrophic motion from higher latitudes towards the equatorial thunderstorms. This picture (illustrated in Grotjahn, 1993, figure 3.22) is tidy but does not address several key questions, such as: Why is the Hadley circulation stronger in the winter hemisphere? How does the local sinking compare with the far field sinking? How much of the tropics has deep convection? How does the Hadley cell transport the heat?

Digging deeper, the concept that the latent heating, even indirectly, generates the Hadley cell might be misleading (Emmanuel, 2000). Much of the tropical troposphere has lapse rate similar to the pseudoadiabatic lapse rate, so one might argue that the latent heating is already in an approximate balance with the cooling from rising motion. Hence, the moist convection creates that environment but if latent heating was the only driver, then one might think the Hadley cell would be stronger in the summer hemisphere since the convection is strongest there. One might expect stronger convection in the summer hemisphere from simple arguments like the Sun being more directly overhead, heating up land areas (or ocean surface) that feeds low-level, large scale convergence. However, to find a strong thermal contrast and hence meridional pressure gradient to drive the ageostrophic motion, one must look beyond the tropics of the summer hemisphere. As discussed later, the rotation of the Earth introduces an angular momentum constraint the meridional extent of the Hadley cell. However, the winter hemisphere subtropics do have a much larger contrast with the tropical temperatures (and pressure field) causing the Hadley cell to be stronger in the winter hemisphere. So, the tropical convection is indirectly maintaining conditions in the tropics while strong net radiative cooling in the winter subtropics sustains a strong contrast with the tropics. Figure 4.6 contrasts the summer and winter hemisphere Hadley circulations.

The summer hemisphere has net radiative warming in the subtropics (Figure 3.12c,f) at the TOA. The temperature gradient in the summer hemisphere is weak as well (Figure 3.20). The winter hemisphere has net radiative cooling at TOA with a strong meridional gradient. The winter hemisphere subtropics has a strong temperature gradient, mainly from 20 degrees latitude poleward within the figure. That high altitude cooling air is easily imagined to sink adiabatically. The adiabatic warming by compression only partially compensates leading to net cooling of the air (e.g. Trenberth and Smith, 2008, figure 5). In this view, the upper level pressure gradient is created by the strong cooling within the winter hemisphere subtropics providing the contrast with

the otherwise quasi-uniform tropical conditions. This view obviously demonstrates how the winter Hadley cell is stronger.

The simple schematic of Figure 4.6 also provides a context to introduce some additional complexity fundamental to the Hadley cell tropical convection. The rising motion is drawn within thunderstorms by necessity for the following reason. The distribution of moist static energy (MSE; see appendix C) inhibits vertical motion except within the lower troposphere. Figure 4.7a,b shows the distribution of $\left[\overline{MSE}\right]$. There is a general tendency for dry static energy (DSE) to increase towards the ICZ (due to warmer temperatures) and to increase with elevation (due to the atmosphere being statically stable so that the gZ term dominates the C_PT term). The dotted lines in the vertical cross sections show that low level air flowing towards the ICZ is gaining DSE. The air flowing towards the ICZ is also being moistened so MSE increases more than DSE. Eventually, the $\left[\overline{MSE}\right]$ rises to values at 1000hPa that exceed corresponding MSE values above until a level near 250hPa (~10km). In regions of preferred climatological convergence (Figure 4.7c,d) the time mean values are another 5-10% higher ($>3.4x10^5$ m^2s^{-2}) than the $\left[\overline{MSE}\right]$ values at 1000hPa. These preferred regions include: southern Amazonia, Congo basin, Australia's Northern Territory, and the island of Papua New Guinea during DJF; while during JJA the regions cover Panama, Bangladesh and northeastern India, and the Philippines (along with adjacent ocean of the so-called Pacific 'warm pool'). So, at low levels the time mean MSE has horizontal variation created by the wind field (convergence) and land-ocean temperature contrasts. In the upper troposphere, the MSE pattern is much smoother. Accordingly, above these preferred regions, the time mean MSE at 1000hPa is comparable to the corresponding MSE at 150hPa (~16km). One can imagine that at specific times, smaller-scale low-level moisture convergence creates even higher MSE values (approaching $3.6x10^5$ m^2s^{-2}) matched again only at even higher levels (e.g. 18km). As discussed in Chapter 3, these extraordinarily deep thunderstorms elevate the tropical tropopause and sustain the 'cold trap' that 'freeze dries' air entering the stratosphere. For air to move through such a great depth it must not be substantially mixing with the lower MSE values of the environment around these clouds. Therefore the upward motion of the Hadley cell is insulated in what Riehl and Malkus (1958) labelled 'hot towers'.

The insulated 'hot towers' cover a far smaller area than is feasible to draw in Figure 4.7. This follows from the asymmetry of rising and sinking motion locally. Bjerknes (1938; summarized in Randall, 2015, p. 168-170) has a brief mathematical explanation. For local mass

balance the upward mass flux within the thunderstorm cores (= $\rho\, w_c\, b_c$) must equal the downward mass flux in the clear air (= $\rho\, w_s\, b_s$) where the b's are the normalized fraction of area of cloudy and sinking regions. Hence, $b_s+b_c=1$. One might estimate the sinking from a simple balance between the vertical advection and the radiative cooling:

$$w_s\Gamma = D_T \tag{4.9}$$

In the middle and lower tropical troposphere, D_T ~ -2K/day and Γ~5K/km giving a vertical velocity estimate of w_s ~ -400m/day. Neglecting organized downdrafts, and horizontal temperature gradients, the temperature tendency equations in the cloud and in the sinking air reduce to

$$\frac{\partial T_c}{\partial t} = w_c\left(\Gamma - \Gamma_m\right) \tag{4.10}$$

$$\frac{\partial T_s}{\partial t} = w_s\left(\Gamma - \Gamma_d\right) \tag{4.11}$$

Within the cloud, the latent heating elevates the temperature of the ambient air if the lapse rate is conditionally unstable ($\Gamma_m < \Gamma < \Gamma_d$). This temperature change makes the air more buoyant and fosters the rising. In the clear air, the sinking also elevates the temperature since $w_s<0$ and $\Gamma_d>\Gamma$. The warming in the sinking environment around the cloud thereby reduces the buoyancy of that rising air within the cloud. For there to be the net rising of the Hadley cell, then the increase of T_c must exceed that of T_s and

$$b_c w_c + b_s w_s = w_H > 0 \tag{4.12}$$

It is understood that all the vertical motions are time and area averages. Subtracting (4.11) from (4.10) yields

$$\frac{\partial\left(T_c - T_s\right)}{\partial t} = w_c\left(\Gamma - \Gamma_m\right) - w_s\left(\Gamma - \Gamma_d\right) \tag{4.13}$$

Using (4.12) to substitute for w_s in (4.13) yields:

$$\frac{\partial\left(T_c - T_s\right)}{\partial t} = \frac{w_c}{1-b_c}\left(\Gamma - \Gamma_m\right) - \frac{w_c b_c}{1-b_c}\left(\Gamma_m - \Gamma_d\right) - \frac{w_H}{1-b_c}\left(\Gamma - \Gamma_d\right) \tag{4.14}$$

One notes that $\left(\Gamma_m - \Gamma_d\right) and \left(\Gamma - \Gamma_d\right) < 0$ and $\left(\Gamma - \Gamma_m\right) > 0$. Also, the updraft velocity is far larger than the Hadley motion if it were averaged over the entire tropical region, so the w_H term in (4.14) is neglected. In order for the convection to be sustained, the left hand side must be positive and thus the first term must be larger than the second term. Thus

$$b_c < 0.5\frac{(\Gamma - \Gamma_m)}{(\Gamma_d - \Gamma_m)} \quad (4.15)$$

The smaller the b_c the larger the T_c-T_s tendency. Hence a small fraction of the area will have the deep thunderstorms. Charney (1963) arrived at a similar conclusion using scale analysis applied to the vertical component vorticity equation to show that dry vertical motion is smaller in the tropics than the higher latitudes and must be concentrated within 'a narrow band' of moist convection. Observations show that 4-10% of the area with ICZ convection is covered by deep convective clouds (Mace et al, 2009). Using 5 m/s as a threshold updraft speed within these hot towers (LeMone and Zipser, 1980) estimate that updrafts covering <1% of the equatorial tropics are sufficient to provide the Hadley Cell rising branch. Thus, local sinking causes tropical thunderstorms to cover about ten times the area needed to sustain the Hadley cell.

4.2 Winds

4.2.1 Hadley Cell Winds

The Hadley cell discussion continues as the emphasis segues to winds while the pressure field recedes from (but remains in) the discussion.

Halley (1686) made the earliest known large-scale chart of the general circulation winds. Halley's chart (reproduced in Grotjahn, 1993, figure 1.1) shows tropical surface winds over the oceans (30S to 30N) and it corresponds well with modern charts. The time mean wind vectors at 950 hPa in Figure 4.8 illustrate the near-surface wind pattern. The arrow length is proportional to the vector wind speed. Since vectors are added to create this figure, areas with short arrows on the chart are not necessarily regions of light winds. For example, equally strong winds that blow half the time from the east and half the time from the west would have zero magnitude on this chart. However, if the wind speed and direction are approximately steady, then the vector average used here approximates the time mean wind speed. Consequently, the figure emphasizes the tropical latitudes over oceans where winds reliably blow in a similar direction and speed during the season. Those tropical ocean winds have been labeled 'trade winds' for centuries due to their reliability for powering sailing ships. Thus, larger arrows in Figure 4.8 in part indicate persistence of wind direction.

From angular momentum conservation considerations in Chapter 1, one expects the equatorward motion to have a westward component. Northeasterly and Southeasterly 'trade winds' are indeed visible over the tropical Pacific and Atlantic oceans.

As noted in connection with Figure 4.5, motion around the equatorial sides of the subtropical highs feeds the low level winds of the Hadley cells. The large scale, time average convergence is also plotted in Figure 4.8. In connection with schematic Figure 4.6, the vertical motion is concentrated in a small fraction of the tropics. The intertropical convergence zone (ICZ) is revealed as these quite narrow bands of low-level convergence. Even these narrow bands are in some sense an exaggeration, as deep, troposphere-spanning convection is only filling 4-10% of the area within these bands (Mace et al., 2009) at any one time.

Precisely-speaking, the Hadley cell is a zonal average circulation and Figure 4.8 shows a lot of zonal variations. To simplify the discussion, 'regional Hadley cell' will be used to label longitudinal portions that are consistent with the zonal mean circulation by that name. The ICZ across the central to eastern Pacific is remarkable in its persistence in nearly the same narrow latitude range year round. This persistence can explain the narrowness and the larger time mean convergence values. In contrast, broader bands: across the southern Indian ocean (DJF and SON) and the South Pacific Convergence Zone (SPCZ) have lower average convergence due to fluctuations in where the ICZ occurs on different days. Areas of convergence over land appear less regular than over oceans, in part due to topographic effects. So, these time mean maps show large ICZ meridional meanders.

Geographical variations reinforce or inhibit the seasonal change at different longitudes. The seasonal change is subtle across the central to eastern Pacific and also in the tropical Atlantic. The eastern Pacific ICZ has little seasonal change mainly because of the persistent sea surface temperatures (SSTs) with cold water upwelling along the equator on a time average and the persistent sea level pressure subtropical high off South America's west coast. The eastern Pacific SSTs change on a longer time scale than seasonally, in part captured under the 'El Nino – Southern Oscillation' umbrella. The regional Hadley cell is more obviously stronger in winter from Africa over the Indian Ocean and into the western Pacific. Figure 4.8 also reveals that one might interpret the Asian summer monsoon over Southern Asia as part of regional Southern Hemisphere Hadley cell whose ICZ is over the continent. That monsoon convergence occurs well north of the equator. Hence, the JJA cross-equator flow over the western Indian Ocean extends over a very large range of latitudes. Finally, it is also clear that the seasonal divisions based on 3-month averages are not symmetric as MAM differs from SON over much of the Eastern Hemisphere.

4.2.2 Zonal Mean Meridional Circulation Perspectives

The Hadley cell is vigorous enough that it shows up when averaging meridional winds over all longitudes and over time. As implied by our thought experiment in Chapter 1 and by the low level winds of Figure 4.8, the Hadley cell extends into the subtropics but not beyond. Is there a zonal and time mean meridional circulation outside the tropics?

Above the boundary layer, the local, instantaneous *zonal* velocity has comparable magnitude to the time and zonal average *zonal* velocity. Such is not the case for the meridional velocity outside the tropics. The zonal mean meridional velocity, [v], has much smaller magnitude (by a factor of 10) than typical velocities measured at individual stations for two main reasons. First, the meridional wind component is approximately geostrophic at these latitudes above the boundary layer. So, when a zonal average is taken, a large part of that average is an integral over all longitudes of a derivative with respect to longitude of a mass field. Since the mass field does not have discontinuities and the integral has an uninterrupted circuit around the earth, the geostrophic portion of the meridional wind does not contribute to [v]. Thus, the zonal mean meridional velocity is an ageostrophic wind. Second, in middle and higher latitudes, as deduced in Chapter 1, the primary circulation consists of eddies with large flows north and south at a given level. However, meridional wind across a latitude circle must be balanced by a wind the opposite direction at another level or longitude otherwise mass would accumulate (or be lost) over time. There is some mass exchange back and forth between the hemispheres seasonally, but the associated net meridional wind is not large. Hence, [v] is small and has been difficult to estimate outside the tropics by direct means because the observational errors and biases have been comparable to [v]. So, some care is needed in order to answer the question posed in this paragraph.

One solution to obtaining [v] is to approach the problem indirectly by exploiting angular momentum (M; eqn. 1.1) conservation with some simplifying assumptions. Namely to neglect: i) mountain torques, ii) friction, iii) any net shift of mass across a latitude circle, and iv) time tendency of M. Dividing a meridional cross section into latitude by pressure ‘boxes’ then the flux of M across one face of the ‘box’ equals the sum of the fluxes across the other three faces. At the highest elevation box at a pole, there is no flux from a latitude higher than the pole and none from above p=0 leaving two remaining box sides to be determined. One uses the continuity equation to expresses the mean meridional vertical motion [ω] in terms of the mean meridional velocity [v]. Then the flux of M through the box bottom is expressed in terms of [v] as is the flux of M through the side box. The key that makes this work is [vM] includes [vu] which can have a geostrophic contribution (as discussed in Chapter 6) and the observational network of the mid

twentieth century and beyond is good enough to estimate [vu] with sufficient accuracy to obtain a midlatitude "Ferrel" cell. Since the formula no longer contains [ω], one solves for [v]. Next, the continuity equation obtains [ω] and the estimates for that box are complete. An adjacent box is solved next and again, two sides of the box are known and one proceeds in this fashion filling every box of the cross section. In practice, directly measured [v] is used in parts of the tropics where the meridional transport by the Hadley cell is strong. Since the continuity equation is two dimensional (2-D), so is the resulting flow, and a 2-D flow can be represented by a stream function. The stream function, ψ can be obtained from the time and zonal mean meridional wind.

$$\overline{[\psi]} = \frac{2\pi R}{g} \int_0^p \overline{[v]}\, dp \tag{4.16}$$

where stream function represents a two-dimensional flow:

$$[v] = \frac{g}{2\pi r \cos\varphi} \frac{\partial [\psi]}{\partial p} \tag{4.17}$$

$$[\omega] = \frac{-g}{2\pi r^2 \cos\varphi} \frac{\partial [\psi]}{\partial \varphi} \tag{4.18}$$

This procedure gives approximate velocity magnitudes, but the resultant stream function gives a useful picture of the circulation patterns.

Modern reanalyses process observations through an atmospheric model having higher order balances than geostrophic. Reanalyses can produce estimates of the mean meridional cells, though they differ with the reanalysis used (e.g. Grotjahn, 2004). Figure 4.9 shows both the vector motion and the stream function in each of four seasons found using winds in a current reanalysis. The stream functions calculated in this way are depicted in Figure 4.9. A constant amount of mass flows between each pair of contours, hence more closely spaced contours indicate faster speed. (The contour interval is not constant in this figure.) The direction of the motion is indicated by the arrows. The most obvious pattern is a three-cell circulation in each hemisphere similar to that envisioned by Ferrel (1856; 1859; 1893).

Six general comments about the detailed structure of the mean meridional circulations in isobaric coordinates follow.

(1) As expected, the meridional circulation is dominated by a thermally-direct Hadley cell in the winter hemisphere. Northern Hemisphere during DJF; Southern Hemisphere during JJA. In both cases the Hadley cell in the summer hemisphere has much less magnitude. During the two other seasons shown, the two Hadley cells have roughly equivalent magnitude.

(2) Also expected, the latitudinal position varies seasonally as well. The winter Hadley cell extends on the winter side to ~30° and crosses the equator with rising centered at 5 to 10° latitude in the summer hemisphere. During MAM and SON, the ICZ is north of the equator, consistent with the regional Hadley cell in the Atlantic and eastern Pacific (Figure 4.8).

(3) A thermally indirect Ferrel cell is seen during all seasons in both hemispheres. The Ferrel cells have significantly weaker circulations than the Hadley cells in this depiction. 'Thermally indirect' means rising where temperatures are relatively colder (at higher latitudes) with sinking where temperatures are relatively warmer (at lower latitudes) with horizontal motion to complete the circuit; hence the opposite flow as a 'Hadley' cell.

(4) The Ferrel cells do not have much variation from season to season in the Southern Hemisphere. However, in the Northern Hemisphere the Ferrel cell is strongest during winter and nearly disappears during summer.

(5) Figure 4.9 has slight evidence of thermally direct polar cells. The polar cells are very weak and this apparent verification of Ferrel's three-cell hypothesis may only be fortuitous coincidence. Some prior calculations of the mean meridional circulation have shown polar cells (e.g. Pauluis et al., 2008), others (e.g. Kjellsson et al., 2014) have not.

(6) The lower level horizontal flow in the cells takes place in a shallow layer near the earth's surface (p>700 hPa) while the upper-level return flow is somewhat concentrated near the tropopause (300 >p> 150 hPa). Hence, examining the flow at 950 hPa (Figure 4.8) or 850 hPa and at 200 hPa (later figures) captures the horizontal flow of these cells.

As discussed in the previous section, Figure 4.9 creates the misleading impression that the ICZ is broad zone of relatively weak rising. Instead, the upward motion is concentrated within thunderstorms in the zone. That is not the only mistaken impression. Another problem was very familiar to William Ferrel. Namely, how does one account for the thermally indirect cell in midlatitudes? The "Kuo-Eliassen" equation (Chapter 9) demonstrates that indirect meridional circulations are driven by eddy fluxes and diabatic fields. For now, the picture is better understood by looking at the mean meridional circulation using alternative vertical coordinates.

Potential temperature (θ) is considered first, then equivalent potential temperature (θ_e). An advantage of θ coordinates is that adiabatic flow is confined to isentropic surfaces (constant θ surfaces). In contrast, adiabatic flow is not limited to surfaces of constant pressure or height. Diabatic processes cause air parcels to migrate from one θ surface to another. If the only diabatic process is latent heat release by condensation, then air parcels stay on constant θ_e surfaces. Time

and zonal mean seasonal distributions of both variables are shown in Figure 4.10. The patterns for these variables are similar to those for dry and moist static energy (Figure 4.7) because the quantities are thermodynamically similar. Potential temperature increases with elevation as expected from large scale static stability and is greater in the stratosphere. The meridional gradient of θ is weak in the tropics and largest in the middle latitudes. Equivalent potential temperature is strongly influenced by moisture in the tropical, lower troposphere. As a result, surface values of θ_e are comparable to values at ~300 hPa in the tropics, with a relative minimum near 650 hPa. Also, θ_e values in the lower (polar regions) to upper (deep tropics) troposphere are clearly higher than θ. The meridional gradient of θ_e is much larger and shifted toward lower latitudes than the corresponding θ gradient. The differing gradient and values result in nearly vertical θ_e contours in middle latitudes and negative θ_e lapse rate in the tropics and subtropics.

Near frontal cyclones, constant θ surfaces dip low where warm air is drawn ahead of surface low pressure and rise high in the cold air behind the low pressure center. Since air moving adiabatically remains on a θ surface, then the mean meridional circulation is more clearly depicted by zonal averaging along constant θ surfaces than p or z. Figure 4.11 schematically shows the motion of air relative to a θ surface near a developing frontal cyclone. This figure reveals how a Ferrel cell in pressure coordinates is actually a thermally direct cell in θ coordinates. In the cold air sector, to the west of the surface low, air is sinking as it moves poleward adiabatically. In the warm sector, to the east of the surface low, air is moving poleward towards a colder air mass and will rise as does the potential temperature surface where it resides. Crucially, the colder air parcel, while higher in z, is lower in θ compared with the warm air parcel.

In broad terms, trajectories follow paths much like the schematic illustration in Palmén and Newton (1969; their Figure 10.20). Palmén and Newton make a pair of simple heuristic arguments for the air mass moving equatorward becoming progressively shallower. Consider the potential vorticity formula in isentropic coordinates (C.49). If the air parcels are restricted from having or developing relative vorticity, then equatorward motion decreases the Coriolis parameter and the pressure spacing between θ surfaces must decrease. The cold air becomes thin enough so surface heating can moderate the air causing the cold front to stall or dissipate. If parcels are turned anticyclonically by descending to the equatorward side of a surface high the cold air layers thin even more rapidly. If the flow were to develop relative vorticity as f decreases, then it develops an eastward component so its equatorward progression again slows.

Only very cold and deep air masses can penetrate beyond 25 degrees latitude (Palmén and Newton, 1969).

When the paths traced out by the warm and cold air parcels in Figure 4.10 are projected onto the meridional plane, then the paths look like a Ferrel cell when height or pressure is the vertical coordinate. When θ is the vertical coordinate, the parcels trace out a thermally direct circulation shown in Figure 4.12a,b. Diabatic processes cause parcels to follow paths that migrate to different elevations of θ seen in the figure.

(1) Since cold air (low θ) sinking behind a cold front is becoming more shallow the further equatorward it moves, it can be more easily warmed by absorbing solar radiation, by exchanging heat with the earth's surface (if it is near the surface), and/or from penetrative convection (if it is not near the surface). Hence, the low level flow has lower θ values that increase along the path toward the equator.

(2) As frontal cyclone warm sector air parcels (middle θ values) reach a front, precipitation forms and consequently latent heat is released. The latent heating increases θ. The result is the paths with increasing θ in middle latitudes. The latent heat release in frontal cyclones is most prominent in broad warm frontal cloud masses. The upward motions near 40 degrees latitude in Figure 4.12a,b correspond well with the location of secondary maximum (annual average) precipitation shown earlier (Figure 1.1a). Seasonal precipitation patterns (Chapter 5) match even better.

(3) At high altitudes and most latitudes, radiational cooling is the dominant diabatic process, causing θ to decrease.

Perhaps the most striking feature about Figure 4.12 is that the indirect, Ferrel cell is missing. Instead of a Ferrel cell, the Hadley cell is extended further poleward by an embedded cell circulating in the same direction. These coincident, thermally direct cells in each hemisphere seem more intuitive since they transport heat poleward as required. (They accomplish this transport since the DSE in the poleward moving upper levels is greater than the DSE of the equatorward moving lower levels, Figure 4.7.)

The stream function in θ coordinates can be decomposed into ageostrophic and geostrophic components. Doing so finds an ageostrophic component primarily in the tropics and geostrophic component primarily in middle latitudes (Townsend and Johnson, 1985).

The mean meridional cells (MMC) in isentropic coordinates can be obtained using the transformed Eulerian mean (TEM) formulation. When the zonal component momentum equation

is zonally-averaged, the result includes both zonal mean flow and divergence of eddy momentum fluxes. (Eddies defined by subtracting the zonal average from each total wind component.) The meridional and vertical motions are 'transformed' by adding a contribution by the meridional heat flux; in turn these define an associated MMC stream function. The eddy fluxes of momentum and heat are separate terms. The TEM stream function (e.g. Juckes, 2001) in ln(p) coordinates closely resembles the MMC in θ coordinates (e.g. Townsend and Johnson, 1985). The TEM formulation yields some advantages: 1) it can reproduce the isentropic thermally-direct circulation in isobaric coordinates and 2) the separate eddy fluxes allows their contributions to the MMC to be isolated. One problem with the formulation is it depends on the vertical coordinate to be monotonic. As Figure 4.10 makes clear, θ_e has a vertical gradient that changes sign in the tropics and part of the subtropics.

By using a 'statistical' extension of the TEM formulation, Pauluis et al. (2011) calculate the MMC in θ_e coordinates while still retaining the ability to separate the heat and momentum fluxes. Figure 4.12c,d shows the circulation in θ_e coordinates. The meridional cell is further simplified, revealing that indeed the rising motion near 40 degrees latitude is due to latent heating (to the extent it can overcome cooling by radiation). Consistent with Figure 4.10, the lower portion of the circulation is at θ_e values that are noticeably higher than corresponding θ values. Paulius et al. also partitioned the heat flux into sensible and latent contributions. In so doing, the single cell in each hemisphere is shown to have somewhat larger contribution by sensible heat flux at higher latitudes: stream function magnitude peaking at latitudes 40-50 degrees, while latent heat flux creates a stream function peaking around latitudes 25-35 degrees.

Schematic Figure 4.11 is based on the growing stage of a frontal cyclone. During the decaying stage, the surface and upper level low centers have migrated away from the frontal zone. Often the surface low merges with or displaces a pre-existing 'semi-permanent' low. Semi-permanent lows are the Aleutian and the Icelandic lows visible in Figure 4.4. The surface high may merge with a subtropical high. A divergent circulation can be imagined as rising near the surface lows (in part by surface friction: Ekman pumping, Chapter 1) with sinking near subtropical highs. This circulation is like a 'regional' Ferrel cell when viewed in isobaric coordinates, at least at upper levels. This motion is a divergent circulation, so it is an order of magnitude smaller than the geostrophic components, hence one argues that even in θ coordinates the 'regional' MMC for the decay stage may be much weaker than where frontal cyclones grow baroclinically. Also, the meridional motions in θ coordinates (e.g. Johnson, 1989; his figure 10a) do not separate vertically during the decaying stage as they do in Figure 4.11. Finally, the

decaying stage eddies transport little sensible or latent heat (Lau, 1978) in the net compared with the growing stage, so one expects little contribution to the MMC in θ coordinates.

As indicated, the Hadley circulation in all three coordinate frames shown is thermally direct. That statement raises the obvious question of how does the Hadley cell transport heat? Figure 3.18 suggests that the net (vertical and zonal average) heat flux is a smaller difference between two larger quantities of opposite sign. There is a net heat transport poleward even though there is no net transport of mass because the potential temperature increases with elevation (i.e. the atmosphere is statically stable). Similarly, DSE (Figure 4.10) is larger at higher than lower elevations, leading to a net sensible heat flux.

The vertical and zonal average sensible heat flux was discussed in §3.2.2. The formula (3.17) can be used to obtain the atmospheric sensible heat flux (ASHF) across a latitude φ within an atmospheric layer Δp thick.

$$ASHF = [\overline{DSE}]\left[\overline{v}\right] 2\pi r \cos(\varphi)\, g^{-1}\, \Delta p \qquad (4.19)$$

where the vertical integral over pressure has been approximated using vertical average values for the layer. From values of [v], one can estimate the net atmospheric sensible heat flux and compare it with observed values. To make a comparison, the transport across 20 N is assumed to occur in an atmospheric column encircling the earth that is divided into northward and southward flowing layers. The meridional flow must have no net transport so [v] = +1 m/s in a layer from 100-400 hPa while the lower layer has stronger [v] = -2 m/s, but is proportionally thinner: 850-1000hPa. From Figure 4.7, a reasonable annual average value for the dry static energy (using upper tropospheric values at 20 N) is DSE $\simeq 3.5 \times 10^5$ J/kg and DSE $\simeq 3.3 \times 10^5$ J/kg for the lower layer. These values imply heat fluxes of $+4.0 \times 10^{16}$ W in the upper layer and -3.8×10^{16} W in the lower layer. The net transport in this simple model is close to the observed values. The observed annual sensible heat transport in the subtropics is about $ASHF = 2.5 \times 10^{15}$ W (Newton, 1972). Thus, only a small amount of the energy being transported at upper and lower levels (~6%) is transported in the net across latitude φ and therefore goes into reducing the pole to equator gradient. In a related way, it will be shown later (Chapter 7) that only a small amount (0.1 to 0.2%) of the potential energy present in the atmosphere is used to drive the general circulation.

4.2.2 Zonal Mean Zonal Wind

The uneven distribution of radiation sets up an uneven distribution of temperature; the

primary variation of both quantities is a meridional gradient. From simple dynamics, the temperature gradient is proportional to wind shear in the orthogonal horizontal direction. Hence thermal wind shear means the general circulation in the middle and upper troposphere is dominated by westerly wind.

Figure 4.13 shows the time and zonal mean zonal wind, $[\bar{u}]$ fields for the extreme seasons. Winds blowing from west to east are $[\bar{u}]>0$. Negative values (winds from east to west) are shaded. Thermal wind shear (westerly wind shear proportional to negative meridional temperature gradient) is also evident with the included zonal and time average potential temperature $[\bar{\theta}]$ contours. The general pattern of $[\bar{u}]$ is described as follows.

Figure 4.13 creates the subjective impression of approximately no net torque applied to the Earth as the area of tropical and Antarctic surface easterlies (shaded) is comparable to the area of surface westerlies. High SLP resides over Antarctica (Figures 4.1 and 4.4) causing easterlies there. Equatorward motion in Hadley cells develops easterlies from angular momentum conservation as anticipated in Chapter 1. The latitude scale of Figure 4.13 exaggerates the area occupied by high latitudes and true angular momentum balance for the Earth also depends on the zonal wind speed (and other factors) but to first order there is approximate balance.

Easterly winds (shaded) occur through the depth of the troposphere in most of the tropical latitudes and in the summer hemisphere stratosphere. A relative speed maximum of easterly wind occurs in the winter hemisphere lower troposphere this extremum is related to the winter hemisphere Hadley cell. The stronger Hadley cell has stronger meridional motion and thus stronger easterly component. During JJA, another easterly speed maximum occurs in the upper troposphere and it will be shown related to an easterly jet stream over the Indian Ocean. Easterly winds are strongest in the stratosphere during summer.

Westerly winds reach several maxima. Each westerly wind maximum in the middle latitudes of each hemisphere at tropopause level near 200 hPa is a 'subtropical jet' stream in the winter hemisphere. These subtropical jets clearly lie above the stronger meridional gradient of potential temperature. Above the subtropical jets the $[\bar{\theta}]$ gradient reverses sign in the lower stratosphere which reverses the vertical shear. The subtropical jets lie at the HCBE boundary (between the Hadley and Ferrel cells of Figure 4.9). Thus, subtropical jet locations visible in Figure 4.13 are ~30N during DJF, ~30S and ~45N during JJA. In the summer hemisphere a jet lies near the tropopause, but close inspection of Figures 4.9 and 4.13 reveals the summer jet is

poleward of the HCBE. Since the summer jet lies in the Ferrel cell, and the Ferrel cell is created by eddy fluxes and diabatic processes, this jet is sometimes called an 'eddy-driven' jet (e.g. Lee and Kim, 2003) or a merged jet (a merger of subtropical and eddy-driven jets, e.g. Lachmy and Harnik, 2014). The so-called eddy-driven jet has been called the 'polar front' jet (e.g. Palmén, 1951; Palmén and Newton, 1969) for many decades. Polar front jets are visible in Figure 4.13: during DJF ~50S and JJA ~70N and ~50S (the latter for p≥450hPa elevation). Notably, the polar front (or eddy-driven or merged) jet occurs year round; its horizontal fluctuations make it less visible in wintertime and zonal averages. (Arguably, the DJF jet in Figure 4.13 near 30N may have contributions from the 'merged' subtropical and polar front jets.) At the highest elevations shown, a polar night jet is found in each winter hemisphere (most easily seen ~60S in JJA at the diagram top). The potential temperature gradient continues into the lower stratosphere beneath each polar night jet. These jets are centered at much higher latitudes than the subtropical jets.

All these velocity maxima occur above regions where there exist strong meridional temperature gradients, as one expects from weaker surface winds plus thermal wind shear. The meridional temperature gradient is often stronger in the upper troposphere for the subtropical jet, but is often stronger in the lower troposphere for the polar front jets. These temperature gradient elevations were also well-known decades ago (e.g. Palmén and Newton). Since the polar front jet is associated with the thermal fronts of a frontal cyclone, the jet location migrates north and south over time and longitude so one should not expect it to be particularly strong on a time and zonal average. In contrast, the subtropical jet is more steady in time as is the Hadley cell and can be captured better with a time average. Also, the polar and subtropical jet streams are not always distinct, but often merge. Since the wind is primarily geostrophic (outside of the tropics), the strongest meridional height gradients also correlate well with the areas of maximum wind speed (Figure 4.1a).

The processes that produce these local enhancements in the temperature gradients are different between the stratosphere and the troposphere. Photochemical processes and the tropopause being highest in the tropics set up the stratospheric temperature gradient (Figure 3.20). The tropospheric jets arise from the mean meridional cells and the midlatitude eddies, as will be detailed in Chapter 9.

Seasonal variations are complex. This stratospheric reversal of wind direction with season could be anticipated from the zonal average temperature fields (Figure 3.20). The seasonal variation of the subtropical jet is also noticeable. The winter jet is stronger (>40 m/s) than the summer jet (SHem: 30m/s; NHem: >20m/s). The jet stream core moves to lower

latitudes in winter, centered at ~30° latitude in winter and ~45° in summer. As with other variables, the seasonal variation of the Northern Hemisphere jet is greater than in the Austral Hemisphere. However, the polar night jet has bigger seasonal change in the Southern Hemisphere. The polar night jet is much stronger in the Southern Hemisphere, reflecting the much colder polar, tropospheric temperatures during winter. The polar night jet is not well identified in Figure 4.13 due to the choice of vertical axis. The location of the polar night jet varies strongly and rapidly with the seasons; its elevation typically ranges from 35 to 60 km (5 to 0.3 hPa) during the winter months (e.g., Hartmann, 1985). During June through August 1979, Lau (1984) finds the maximum wind speed at 50 hPa to be about 52 m/s.

If eddies try to build time mean [u] poleward of the HCBE by momentum convergence, then the meridional flux of zonal mean absolute vorticity, opposes the change. To show this, one can partition the wind components due to zonal average and eddies (deviations from zonal mean) in the zonal component momentum equation (C.26) in Cartesian and isobaric coordinates:

$$\frac{\partial\left([u]+u'\right)}{\partial t}+\left([u]+u'\right)\frac{\partial\left([u]+u'\right)}{\partial x}+\left([v]+v'\right)\frac{\partial\left([u]+u'\right)}{\partial y}+\left([\omega]+\omega'\right)\frac{\partial\left([u]+u'\right)}{\partial p}=fv_a$$

(4.20)

Here, v_a is defined using a variable Coriolis parameter for the geostrophic wind definition for convenience. The continuity equation (C.30) is used to write meridional and vertical advections in (4.20) into flux form. Applying a zonal average eliminates all eddy/zonal mean cross product terms to obtain:

$$\frac{\partial[u]}{\partial t}+[v]\frac{\partial[u]}{\partial y}+[\omega]\frac{\partial[u]}{\partial p}+\left[\frac{\partial v'u'}{\partial y}\right]+\left[\frac{\partial \omega'u'}{\partial p}\right]+\left[u'\left\{\frac{\partial v'}{\partial y}+\frac{\partial \omega'}{\partial p}\right\}\right]=f\left[v_a\right] \qquad (4.21)$$

Assuming the divergence multiplied by the eddy zonal wind is negligible compared to other terms and dropping the time tendency of the eddy zonal wind obtains:

$$\frac{\partial[u]}{\partial t}=[v_a]\left\{f-\frac{\partial[u]}{\partial y}\right\}-[\omega]\frac{\partial[u]}{\partial p}-\left[\frac{\partial v'u'}{\partial y}\right]-\left[\frac{\partial \omega'u'}{\partial p}\right] \qquad (4.22)$$

Assuming we are at jet stream level (to ignore $[\omega]$) and at that level the vertical eddy flux is much smaller than the horizontal (Dima et al., 2005) leaves:

$$\frac{\partial[u]}{\partial t}=[v_a]\left\{f-\frac{\partial[u]}{\partial y}\right\}-\left[\frac{\partial v'u'}{\partial y}\right] \qquad (4.23)$$

If the center of the subtropical jet is at the HCBE, then $[v_a]=0$ since that spot is at the boundary between the Hadley and 'Ferrel' cells. If the jet does not change magnitude over time then the tendency term vanishes in (4.23) and the eddy momentum flux term must be zero or negligible

and cancelled by terms neglected. Poleward of the subtropical jet, eddies are present, perhaps eddy momentum convergence could create a local change of $[u]$ and move the *zonal average* jet axis poleward? The horizontal eddy momentum convergence (second term on the RHS of (4.23) would be positive. But, $[v_a]<0$ there and the horizontal shear, $\partial[u]/\partial y<0$, reinforces the Coriolis parameter to make the first term on the RHS of (4.23) negative and oppose that change in $[u]$. On either annual or seasonal averages, both terms on the RHS are larger in the upper troposphere but nearly cancel (Dima et al., 2005). The planetary boundary layer (where the first term balances frictional drag upon zonal momentum) could be different. The cancellation poleward of the subtropical jet is consistent with maintaining thermal wind balance as will be shown when discussing the 'Kuo-Eliassen' equation (Chapter 9).

Chapter 1 has a general discussion of baroclinic instability where the instability (and hence the growth rate of an eddy) is proportional to the meridional temperature gradient, and hence the zonal wind vertical shear. One might expect the strong shears of the subtropical jet to favor eddy growth at the subtropical jet location and some linear models find that (e.g. Baines and Frederiksen, 1978). Nonlinear idealized studies find that eddies form on an initial jet but through their upper level momentum fluxes build a jet at a higher latitude (initially 40N migrating to 45N in Simmons and Hoskins (1978); initially 45N going to 50N in Grotjahn and Lai, 1991). However, the process is a bit more subtle as static stability and the variation of the Coriolis parameter play important roles in linear growth rates. In addition, actual frontal cyclones can intensify fronts not just move them and cause polar front jets to curve into much higher latitudes than the subtropical jet. And it is long known that additional frontal cyclones can develop along these fronts (Petterssen, and Smebye, 1971; Grotjahn, 2005). In addition, Lee and Kim (2003) show that instability and eddy growth only occurs at the subtropical jet if that jet has sufficiently large vertical shear to overcome the stabilizing effect of the Coriolis parameter. 'Weak' subtropical jets (with jet core speed <50m/s for their parameter choices) have greater linear growth rate 20-30 degrees poleward of the subtropical jet. The growth rate can be estimated from the linear instability study of Eady (1949)

$$Eady\ growth\ rate\ estimate = 0.33098 \left\{ \frac{f}{\sqrt{N^2}} \frac{d\overline{[u]}}{dz} \right\} \qquad (4.24)$$

Furthermore eddies are able to create a zonal mean jet from an initial state that does not have a jet (e.g. Williams, 1978).

4.2.3 Zonal Variations of Jets and Divergent Circulations

To represent the horizontal variations of the jet streams, the 200 hPa level is shown in Figure 4.14. Zonal variations of the subtropical jet streams are linked to height and wind patterns discussed above. Consistent with geostrophic balance, the winds are stronger where the horizontal gradient of time mean geopotential height is stronger (Figures 4.2 and 4.3). That gradient is often stronger at the bases of long wave troughs in geopotential (and temperature, Figure 3.24). Jet stream relative maxima occur near the east coasts of Asia and North America (year around), Australia and South America (during local winter), and south of Africa (during local summer).

The NHem subtropical jet near the east coast of Asia is stronger than the corresponding jet near North America. The largest velocities, off the east coast of Asia, average in excess of $70 ms^{-1}$! These NHem maxima are much stronger during winter (DJF). The downstream end of each of these maxima is further poleward than the upstream end. One explanation invokes how eddies have their upper level momentum convergence stronger at later stages in their life cycle and located both downstream and poleward of their initial latitude (Simmons and Hoskins, 1978) and their initial latitude may have been at the subtropical jet (Blackmon et al., 1977). An argument could be made that as a frontal cyclone pushes warm air ahead, it builds an upper level ridge moving the thermal front (and stronger winds aloft) poleward. The lower troposphere trough develops a poleward motion along this ridge as well. Consequently, two jets occur at some longitudes: one considered subtropical and the other considered eddy-driven (Eichelberger and Hartmann, 2007). On the time mean two velocity maxima occur, one south of the other, over the eastern Pacific and the eastern Atlantic. This combination of velocity maxima contributes to sinking above the east side of the SLP subtropical highs as will be evident when the divergent circulation is shown and from the zonal momentum equation.

The SHem jet streams are more zonally-oriented but still have a poleward bend (southeast Pacific). In summer there is a tendency for stronger flow south of Africa. In winter (JJA) the stronger winds occur east of Australia. The largest average velocities in the Southern Hemisphere just exceed 50 ms^{-1}. As anticipated from the zonal mean (Figure 4.13) there is a secondary maximum at a higher latitude (south of New Zealand and also in the southern Indian Ocean). The more southerly maxima are downward expressions of the stratospheric polar night jet. The dominant jet maximum covers nearly the same longitudinal range as the weaker East Asian jet during JJA. The similar longitudinal locations arise because these jet maxima are

linked with the areas of greatest outflow from intense near-equator convection. The match is not coincidence and can be understood using Rossby wave source arguments (later in this chapter).

Zonal variations in the time mean westerly flow in the upper troposphere can be related to ageostrophic meridional velocities. Following Namias and Clapp (1949) the zonal momentum equation after taking a time average and neglecting vertical and meridional advection relative to the zonal advection. (i.e. Conditions as follows: i) at tropopause level where time average vertical motion is neglected and thus the vertical advection term is neglected. ii) the zonal variation needs to be comparable to or less than the meridional variation of $\bar{u}$ and the advecting velocities $\bar{u} > \bar{v}$.) Friction is also ignored. What remains is a simple balance between the ageostrophic flux of planetary vorticity and the advection of zonal wind:

$$\bar{u}\frac{\partial \bar{u}}{r\cos(\varphi)\partial\lambda} = f\bar{v} - \frac{\partial \overline{\Phi}}{r\partial\varphi} = f\left(\bar{v} - \overline{v_g}\right) = f\,\overline{v_a} \qquad (4.25)$$

Here, v_g is the geostrophic meridional wind. The geostrophic part of the Coriolis term cancels the pressure gradient term and what remains is the ageostrophic component (v_{ag}) by definition. If one approximates the ageostrophic wind by the divergent wind, then (4.25) indicates that poleward ageostrophic (divergent) wind will accelerate the zonal wind downstream (to the east). Similarly, equatorward winds are associated with deceleration of the zonal winds. Returning to the eastern Pacific and Atlantic, the NHem jet streams have an accelerating jet equatorward of a decelerating jet. The associated divergent flow has convergence (in the meridional plane) aloft and that implies sinking on the eastern sides of the corresponding subtropical highs (Figure 4.4).

Divergent winds are *not* the same as ageostrophic winds (gradient winds differ from geostrophic winds, for example). However, to be consistent with later figures, we approximate the ageostrophic meridional wind with divergent wind vectors in Figure 4.14. There is some evidence for the approximate balance of (4.25) with a poleward component of divergent wind often where there is acceleration of the time mean winds and an equatorward component of divergent wind where there is deceleration. Exceptions occur for divergent wind, but there is more agreement with (4.25) than not.

The full picture of the divergent flow is shown in Figure 4.15. The divergent wind vectors reach significant magnitudes. (The largest are >10 ms^{-1}, off the east coast of Asia. More typical maximum values are about 5 ms^{-1}) at this pressure level. As anticipated, the poleward ageostrophic velocities occur where the jets are increasing downstream and vice versa.

The divergent wind field is dominated by huge centers of positive and negative extrema in velocity potential, χ. The Laplacian of velocity potential equals the divergence, hence negative

maxima of χ are areas of divergence. While the divergence is a rather noisy field, especially over land areas (as may be estimated from Figure 4.8) inverting the Laplacian to obtain χ is a smoothing operation that reduces greatly the short-distance variations. The prominent outflow centers are the far western Pacific and Central or northern South America. The north Pacific storm track is strong enough to create its own center of divergence aloft. Major convergent regions aloft overlie desert regions of the subtropics and the subtropical oceans. The implied sinking is consistent with i) the generally clear sky and dry (and hot) deserts as well as ii) low level stratus (Chapter 5) over adjacent oceans. Ageostrophic convergence aloft over the eastern NHem oceans, mentioned above, is an example of this generalization. One must be cautious about inferring MMCs from these ageostrophic motions (Blackburn, 1985), but for a general discussion such inferences are useful. It is immediately obvious that portions of these major divergent centers are regional Hadley cells, including being stronger for the winter hemisphere regional Hadley cell. Judging by the meridional component at the equator, the winter Hadley cell (southward flow) is visible at all longitudes during JJA. During DJF most longitudes at the equator have northward flow though some small longitude ranges do not. It is also apparent that large regions have west-east over turnings, including the 'Walker' cell spanning much of the equatorial Pacific.

Diverging arrows in Figure 4.15 imply rising motion below. Following the divergent wind vectors appears to connect areas of preferred rising with the sinking. The strongest areas of divergence overlie Southeast Asia, Indonesia, and Amazonia. In northern summer, the Walker circulation apparently connects rising motion (and thus precipitation) over the far western Pacific with enhanced sinking over the east side of the subtropical high in the eastern tropical Pacific. The rising air is fed by low level convergence and that results from ageostrophic motions that occur for relatively low surface pressure (Figure 4.4). Low pass filtered observations (Grotjahn and Osman, 2007) show a correlation between heavier precipitation in Indonesia, lower pressure there, and stronger Pacific subtropical highs

The divergent winds of the Hadley cell advect angular momentum poleward. As the planetary contribution to M decreases, the U_{amc} contribution to M must increase and thereby accelerate the flow to form the subtropical jets. The intensity of this mechanism varies regionally. So, the prominent outflow region in the western tropical Pacific is associated with the strongest jet streams: east coast of Asia in DJF and over Australia in JJA. The process can be further understood by considering the "Rossby wave source" (Sardeshmukh and Hoskins, 1988).

The Rossby wave source, S_R, is defined from terms in the vertical component vorticity equation:

$$\frac{\partial \zeta_a}{\partial t} + \mathbf{V}_\psi \cdot \nabla \zeta_a = -\mathbf{V}_\chi \cdot \nabla \zeta_a - \zeta_a D \equiv S_R \tag{4.26}$$

Here the subscript 'ψ' refers to the rotational part of the wind and 'χ' to the divergent part of the wind. Tilting and vertical advection terms are neglected by assumption near the tropopause level. S_R equals the divergence term and the advection of absolute vorticity by the divergent winds. Since the rotational winds contain all of the relative vorticity, the LHS of the equation moves absolute vorticity (ζ_a) around but does not create ζ_a while the remaining terms in S_R can be a source or sink of ζ_a. By making this partition one can see the effect of divergent flow upon a horizontal stream function and the rotational flow. Larger values of rotational flow are greater than larger values of divergent flow. Stream function is a useful depiction of the main flow patterns of the tropics and a proxy for mass field in the subtropics. Consequently, the rotational flow is a proxy for the subtropical jet.

In this example, the large outflow (Figure 4.15) during DJF is centered over a region centered on New Guinea and the Solomon Sea and hence, south of the equator. The outflow is associated with a tropical maximum in precipitation that has a large net release of latent heat of condensation. Figure 4.16 illustrates the situation schematically.

At location R: The deeper tropical thunderstorms might suggest that the stream function be most amplified by the latent heating below. While D is largest here, S_R is not large because both the relative vorticity and the Coriolis parameter are small near the equator and the divergent winds vanish where D peaks.

At location A: The anticyclone is created here. The divergence is small making the divergence term small. But D~0 implies the divergent winds are largest here and have a northward component. Since the meridional gradient of planetary vorticity is positive making S_R is positive and maximized.

At location T: A trough is created here near and above the cold eastern edge of Asia at middle and high latitudes. The divergent wind tends to have a rather small meridional component. But, the divergence is strongly negative as air sinks above the east side of the Siberian high. Hence, S_R is strongly negative and thereby reinforces a trough.

At location J: Between the midlatitude trough and the tropical anticyclone the stream function contours are compressed leading to local intensification of the subtropical jet. Divergent winds blowing northward from the Indonesia region during northern winter

are also consistent with the acceleration of the time mean zonal wind as illustrated by relationship (4.25). The divergent flow southward from the Indonesia region during JJA contributes to the stronger jet over Australia by similar reasoning.

Sardeshmukh and Hoskins (1988) force a barotropic vorticity equation model with diabatic heating centered over New Guinea with diabatic cooling centered over southeast China; their solutions produce the stream function features observed in this region (Figure 4.17). The lower heights to the northwest (location T) are also due to orography. Valdes and Hoskins (1989) use a linear stationary wave model and estimate the long-wave created by orography alone to be about 30% of the observed long-wave amplitude over East Asia. A ridge is also produced in the opposite hemisphere during the opposite season. The diabatic heating enhances the jet stream over Australia during their winter by building a ridge along 10 S between Africa and 170 E. The dominance of the latent heating over Southeast Asia out to the western Pacific explains why the winter subtropical jet is maximum at a similar longitude in both hemispheres. Sardeshmukh and Hoskins (1988) derive an integral constraint by integrating the vorticity equation along a closed ψ contour and applying the divergence theorem; the constraint shows that the ψ maximum must be displaced from the χ maximum. The time evolution of the stream function is likely more complex than the stationary pattern of Sardeshmukh and Hoskins (1988). The tropical convection over the Indian Ocean across to the east of New Guinea can be enhanced by a low frequency wave train emanating from Eurasia and can in turn spur a wave train back into midlatitudes (e.g. Lau and Philips, 1986; Adames and Wallace, 2014) in addition to enhancing the SE Asian subtropical jet. Tropical-midlatitude interactions is a major subfield of meteorology beyond the context of this chapter; a review is presented by Stan et al. (2017).

The zonal mean observations also contain a tropical easterly jet. From Figure 4.13, the largest easterly winds are in the stratosphere. However, easterly wind maxima are identifiable at 200 hPa and are usually centered between east Africa and Indonesia (Figure 4.14) and the maximum exceeds 20 ms^{-1} on a summer-long average.

4.2.4 A Simple Model Connecting Hadley Cell, Angular Momentum, and Subtropical Jet

To conclude this sub-section, a simple model is devised that can explain some gross features of the $[u]$ field. The description of the jet entrance region relies upon poleward ageostrophic motion. From angular momentum conservation, poleward moving air experiences westerly acceleration relative to the ground. The model employs angular momentum conservation,

vertically varying friction, and a Hadley cell meridional motion. The model is only intended to show the westerly acceleration. The model is too simplistic for the Hadley cell because vertical motions are not incorporated directly and it is assumed that the only flows are zonal average (i.e. zonal deviations, 'eddies' are ignored). However, a conceptual picture of the vertical motions could be that all parcels move up or down in thin layers at the north and south boundaries and a *fraction* of the interior air parcels at each latitude sink or rise so as to maintain mass continuity.

One can write the zonal mean angular momentum per unit mass as

$$[M] = [R_C(\Omega R_C + u)] \tag{4.27}$$

Here, ρ is the air parcel density, Ω is the angular velocity of the earth, $R_C = r \cos\varphi$ and r is the earth's radius. Ignoring mountain torques, and eddy fluxes, a conservation law for $[M]$ becomes

$$\frac{d[M]}{dt} + R_C[F_x] = 0 \tag{4.28}$$

Friction is modeled using a Rayleigh formulation.

$$F_x = -k_R u \tag{4.29}$$

where Rayleigh coefficient, $k_R < 0$. This form of friction means that the local derivative and frictional terms in the zonal momentum equation are related as $\partial u / \partial t = k_R u$ which has exponentially decaying solutions for negative Rayleigh coefficient, k_R. For illustrative purposes a 'planetary boundary layer' value of k_R (k_{Rb} = –0.155274 days^{-1}) is chosen for the equatorward flow. Frictional decay in the poleward flow of our "Hadley" cell would be much less. Reasoning by analogy with scaling arguments for Ekman layers in theoretical models (e.g., Grotjahn et al. 1995), k_{Rf} = –4.16 x 10^{-3} days^{-1} is used here.

Substituting (4.27) and (4.29) into (4.28) yields

$$([u] + 2R_C\Omega)\frac{dR_C}{dt} + R_C\frac{d[u]}{dt} = k_R R_C[u] \tag{4.30}$$

Following the motion, the total derivative can be transformed into a latitudinal derivative; time (t) is equivalent to a latitude location (φ) that differs from the starting point (t = 0 and $\varphi = \varphi_0$).

$$\int_0^t [v]d\tau = r\int_{\varphi_0}^{\varphi} d\varphi \tag{4.31}$$

$[v]$ is set to a constant in space and time, leaving

$$dt = \frac{r}{[v]}d\varphi \tag{4.32}$$

After substituting (4.32) into (4.30), the factor $[v]\cos\varphi$ is divided out to obtain

$$\frac{d[u]}{d\varphi} - [u]\underbrace{\left(\tan\varphi + \frac{k_R r}{[v]}\right)}_{G} = \underbrace{(2\Omega r \sin\varphi)}_{H} \tag{4.33}$$

Equation (4.33) is a linear first order ordinary differential equation. The general solution (e.g., Beyer, 1984; p. 315) of (4.33) is found by integration from an initial state with zonal velocity u_0. The general solution is

$$u(\varphi) = \exp\left(-\int_{\varphi_0}^{\varphi} G(\varphi)d\varphi\right) \times \left\{u_0(\varphi_0) + \int_{\varphi_0}^{\varphi}\left(H(\varphi)\exp\left(\int_{\varphi_0}^{\varphi} G(\varphi)d\varphi\right)\right)d\varphi\right\} \tag{4.34}$$

Evaluating the integrals of G yields

$$\begin{aligned} u(\varphi) &= \exp\left(\frac{rk_R(\varphi-\varphi_0)}{[\upsilon]} - \ln(\cos\varphi) + \ln(\cos\varphi_0)\right) \\ &\times\left\{u_0(\varphi_0) + \int_{\varphi_0}^{\varphi} 2\Omega r\sin\varphi\exp\left(-\frac{rk_R(\varphi-\varphi_0)}{[v]} + \ln(\cos\varphi) - \ln(\cos\varphi_0)\right)d\varphi\right\} \end{aligned} \tag{4.35}$$

The integrals in (4.35) can be evaluated numerically using a sum of trapezoids and small increments of latitude. It is useful to consider the time-dependent form of (4.35) by substituting in (4.32). The result is

$$\begin{aligned} u(\tau) &= \exp\left(k_R\tau - \ln\left(\cos\left(\frac{[v]\tau}{r} + \varphi_0\right)\right) + \ln(\cos\varphi_0)\right) \\ &\times\left\{u_0(0) + \int_0^{\tau} 2\Omega\sin\left(\frac{[v]t}{r} + \varphi_0\right)[v]\exp\left(-k_R\tau + \ln\left(\cos\left(\frac{[v]t}{r} + \varphi_0\right)\right) - \mathrm{In}(\cos\varphi_0)\right)dt\right\} \end{aligned} \tag{4.36}$$

Several cases are now examined.

The first case has no change of latitude. Since $[v] = 0$ and $\varphi = \varphi_0$, one must use the form given in (4.36). The integral in (4.36) vanishes in this case, leaving simple exponential decay of the velocity, $[u(\tau)] = [u(0)]\exp(k_R\,\tau)$.

Another special case excludes friction. Either (4.35) or (4.36) may be used, but the velocity profile is independent of time at a given latitude, so it is instructive to use (4.35). The velocities change rapidly with latitude to compensate for the changing planetary rotational velocity. This solution is plotted in Figure 4.18a (for poleward motion) and 4.18b (for equatorward motion).

A more general, third case is poleward motion in the upper troposphere (using k_{Rf} and $[u]$ = –10 m/s at the equator). Several choices of $[v]$ are plotted in Figure 4.18a. For slower meridional motion, the Rayleigh friction has more time to reduce the wind speed. For the value of k_{Rf} used here, a northward motion of 3 cm/s at 30 N results in $[u]$ ($\simeq$ 35 m/s) that is close to

the observed value. But 3 cm/s is about an order of magnitude smaller than the annual and vertical average observed [v] in the upper branch of the Hadley cell (Figure 4.9).

Equatorward flow is occurring in the surface boundary layer. Figure 4.18b ($k_R = k_{Rb}$) shows solutions that commence at 30 N with [u] = 10 m/s. Reasonable zonal velocities occur for much larger meridional velocities than in the third case because friction is now much stronger. These admittedly crude estimates of friction still allow [v] velocities that are comparable with observed values without creating unrealistically large (negative) values of [u]. In short, if the free atmospheric friction is increased in the simple model here, then the observed [u] and [v] profiles in the tropics and subtropics can be reasonably matched, along with the required heat transports.

Of course this analysis also provides another simple explanation for why the subtropical jet would lie between the Hadley and Ferrel Cells as [v] reverses sign implying not just no further poleward advection of higher M air, but actual advection of lower M air from higher latitudes.

However, the derivation above ignored eddy fluxes, when in fact those are large. The equation provides a hint at more detailed discussion (Chapter 9) after a more thorough discussion of momentum (Chapter 6). Beginning with the inviscid zonal momentum equation in Cartesian geometry, using the continuity equation to write it in flux form, then taking time and zonal averages yields an equation that gives a hint of things to come:

$$\left[\overline{\frac{\partial uv}{\partial y}}\right]+\left[\overline{\frac{\partial u\omega}{\partial p}}\right]=\frac{\partial\overline{[u][v]}}{\partial y}+\underbrace{\frac{\partial\overline{[u][\omega]}}{\partial p}}_{K}+\underbrace{\frac{\partial\overline{[u'v']}}{\partial y}}_{L}+\underbrace{\frac{\partial\overline{[u'\omega']}}{\partial p}}_{N}=f\overline{[v]} \qquad (4.37)$$

The term coming from the meridional advection has a MMC part (K) as well as an eddy part (L). Also, the vertical advection term could be further split so that term K be written as [u]∂[w]/∂p and [ω]∂[u]/∂p where the latter part is approximately [ω]∂[θ]/∂y. Thus, the mean meridional temperature gradient is introduced into zonal momentum since the thermal wind shear relationship is a reasonable approximation at these subtropical jet latitudes. The analysis is treated in much greater depth later, using the Kuo-Eliassen equation to show how eddy fluxes of heat and momentum along with diabatic processes contribute to generating an MMC in the isobaric context.

To summarize this chapter, diabatic processes and temperature patterns discussed in Chapter 3 set up patterns of mass that have pressure gradient forces to accelerate the winds. The winds in turn attempt to reduce the temperature gradients by transporting heat. Various constraints reviewed in Chapter 1 along with complex variations of the surface (topography;

land, sea and ice; vegetative cover) lead to a complex circulation. However, many of the elements anticipated in Chapter 1 ‘thought experiments’ are broadly visible in the observed circulations. The conceptual “Hadley cell” bridges very large scale to convective scale motions: there cannot be a broad upward-moving segment but instead a small fraction of the rapid upward motion in tropical thunderstorms, not canceled by sinking adjacent to those storms, is the rising branch. “Hadley cell” meridional heat transport is the smaller difference between much larger opposite transports in upper and lower troposphere, with longitudinal variation showing both preferential rising over specific tropical landmasses and also east-west over-turnings. Zonal wind zonal variation is linked to ageostrophic meridional winds that in turn are linked to tropical convection plus sinking at higher latitudes. Jet streams come in several variants, based on their driving mechanisms. Zonally-varying motions (‘eddies’) dominate the middle and higher latitude circulation. So, eddy momentum covariances are among the main drivers of the conceptual “Ferrel cell”. The Ferrel cell looks thermally-indirect in pressure or elevation coordinates, but for coordinates more aligned to actual air motions: the middle latitude circulation is thermally-direct in potential or equivalent potential temperature coordinates. Eddies form polar front jets (among several names) while MMCs place subtropical jets at the HCBE boundary. However, these jets organize eddies into storm tracks wherein eddies prefer to initiate, grow to maturity, and decay. (Eddy ‘instability’ is explored further in later chapters.) Since eddies create fronts and associated jet streams, eddies are both influenced by the zonal mean and influencers of the zonal mean flow.

Figures

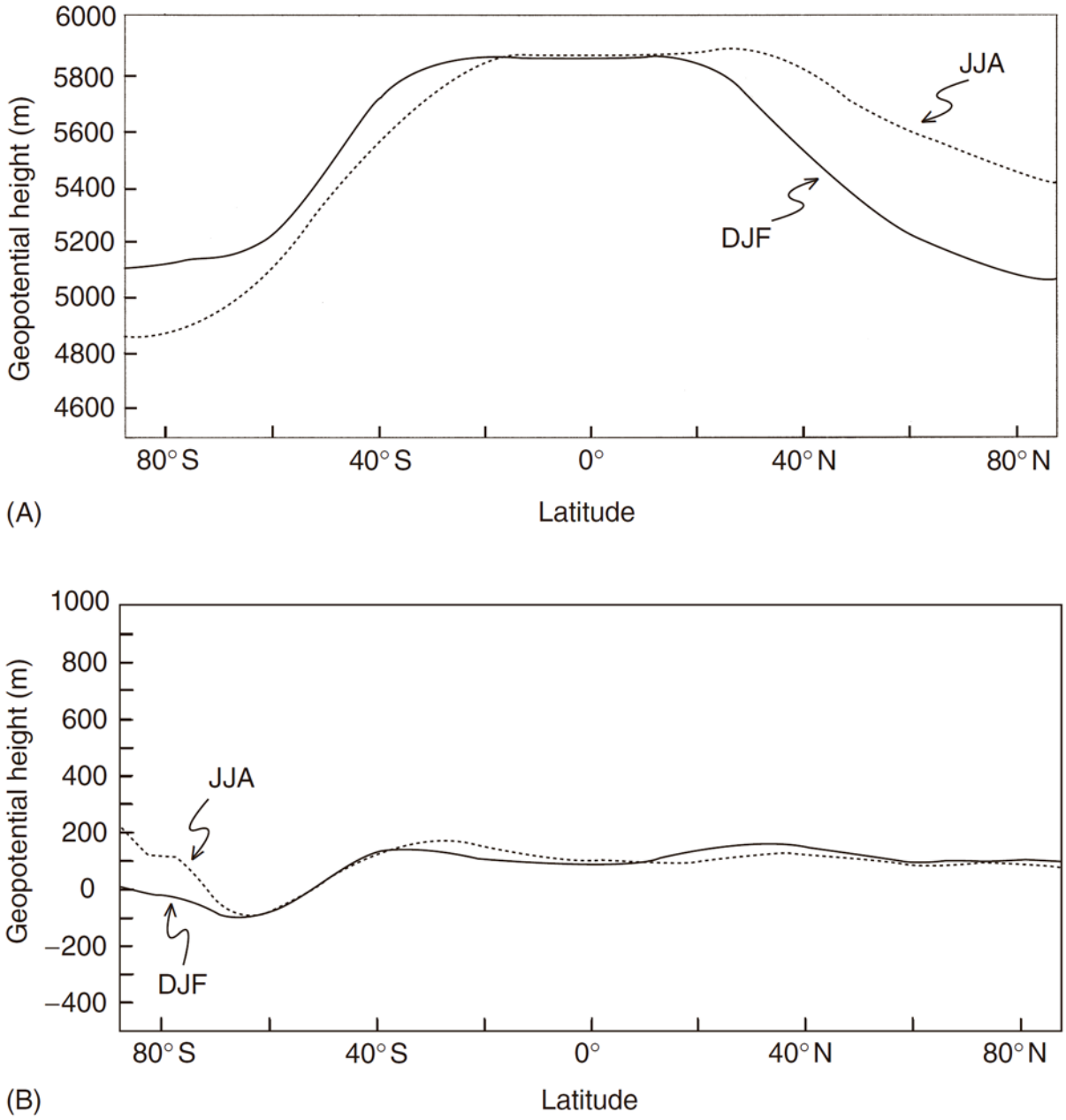

Figure 4.1. Zonal mean geopotential heights (a) at 500 hPa and (b) at 1000 hPa. Solid line is for December–February seasonal average and dotted line is for June–August. These NCEP/NCAR reanalysis data are from 1979 to 1999. Figure reproduced from Grotjahn (2015).

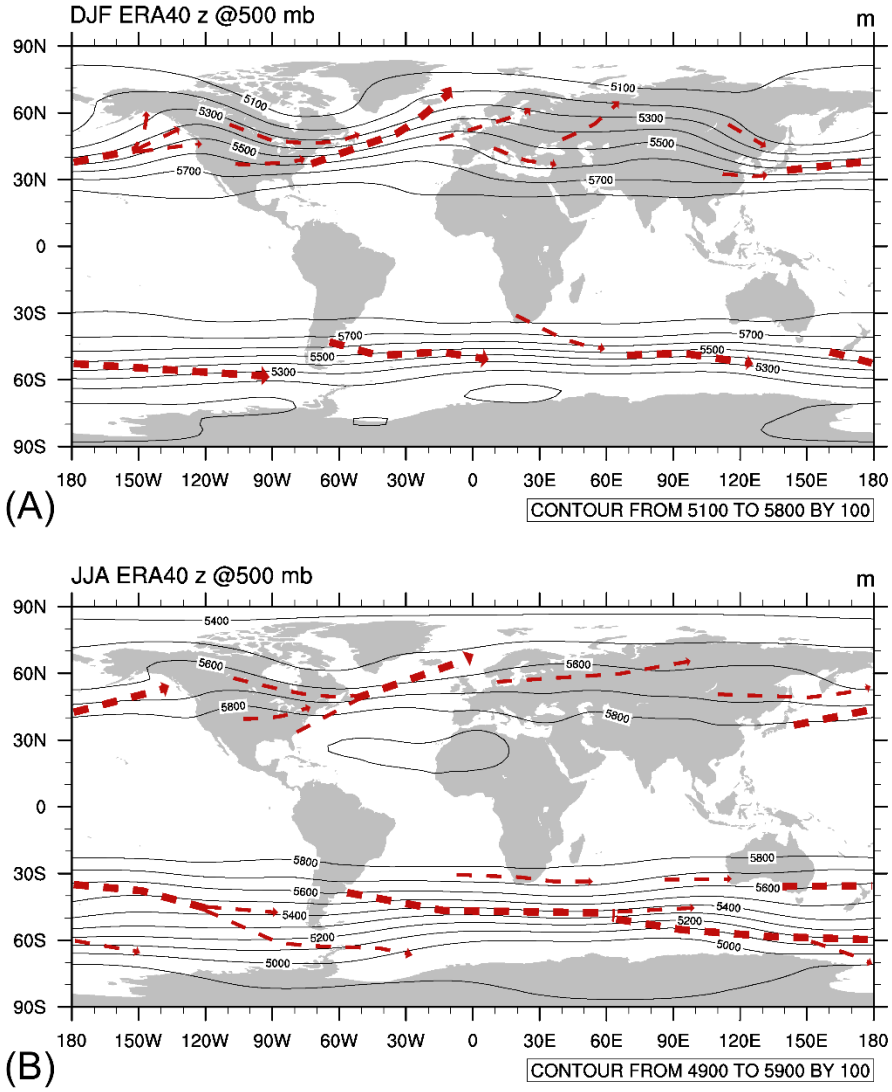

Figure 4.2. Seasonal mean geopotential height at 500 hPa (Z_{500}) from years 1979-2000 (ERA-40 data). Also plotted are general indicators of the frontal cyclone storm tracks (dashed arrows) where a wider arrow indicates more frontal cyclone passages than for a thinner arrow. Reproduced from Grotjahn (2015). Frontal cyclone storm tracks shown merge information from these sources: van Loon (1966), Whitaker and Horn (1984), Simmonds and Murray (1999), Hoskins and Hodges (2002, 2005), Mesquita et al. (2008).

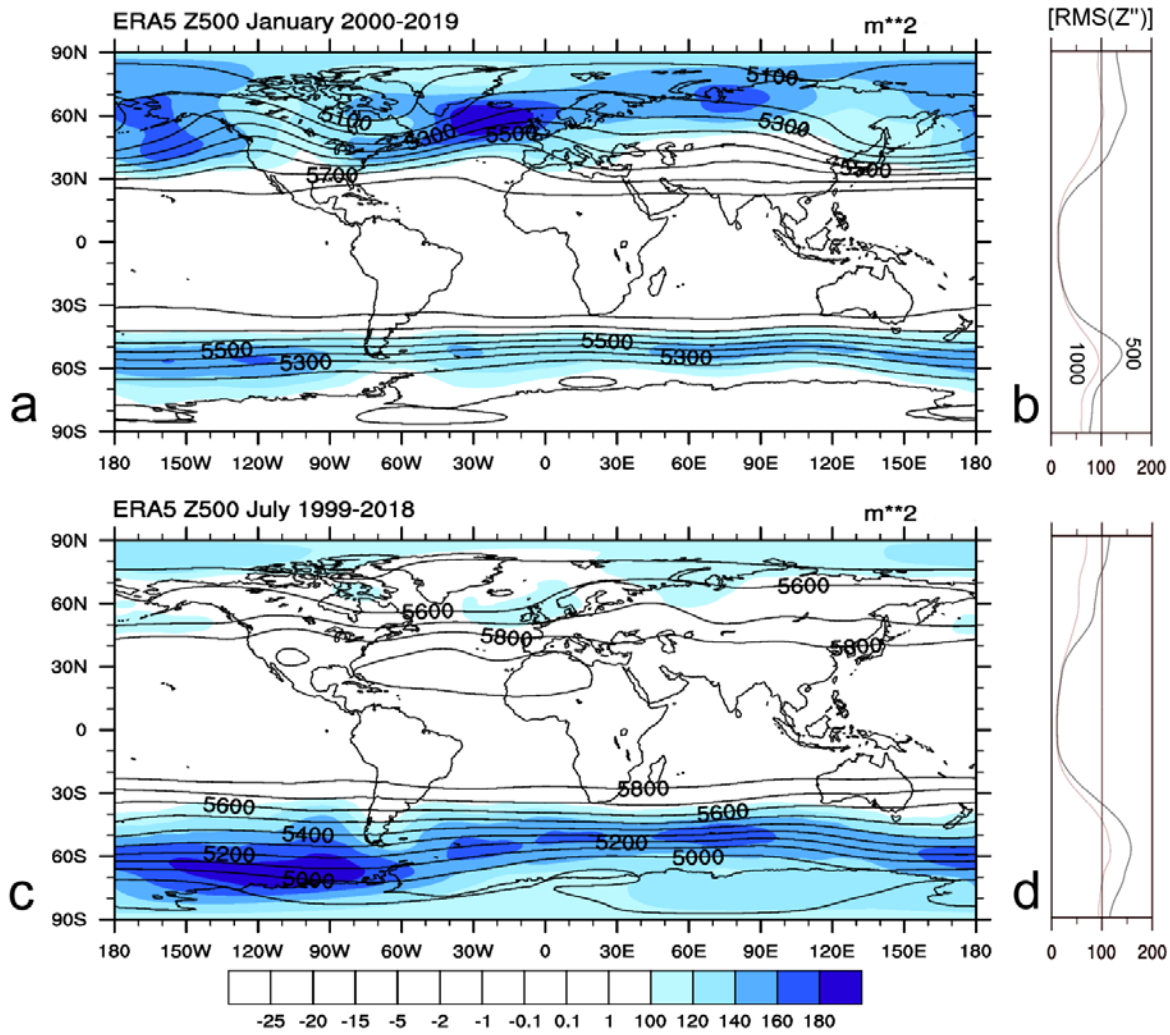

Figure 4.3. (a) January and (c) July seasonal time averages of Z_{500} (contours) and RMS of time-varying 500 hPa geopotential height (shading). The shaded quantity is an imperfect indicator of the storm tracks and adds information to the paths shown in Figure 4.2. The shading emphasizes the mature stage of eddies but not the genesis or lysis stages; also, transient planetary waves are not excluded. The panels to the right, for (b) January and (d) July are zonal averages of RMS time-varying heights at two levels: [RMS($Z"_{500}$)] (thicker line) and [RMS($Z"_{1000}$] (fainter line). [RMS($Z"_{500}$)] > [RMS($Z"_{1000}$)] everywhere. Units are m. European Centre for Medium-Range Weather Forecasts, ERA-Interim data 1999-2017 shown.

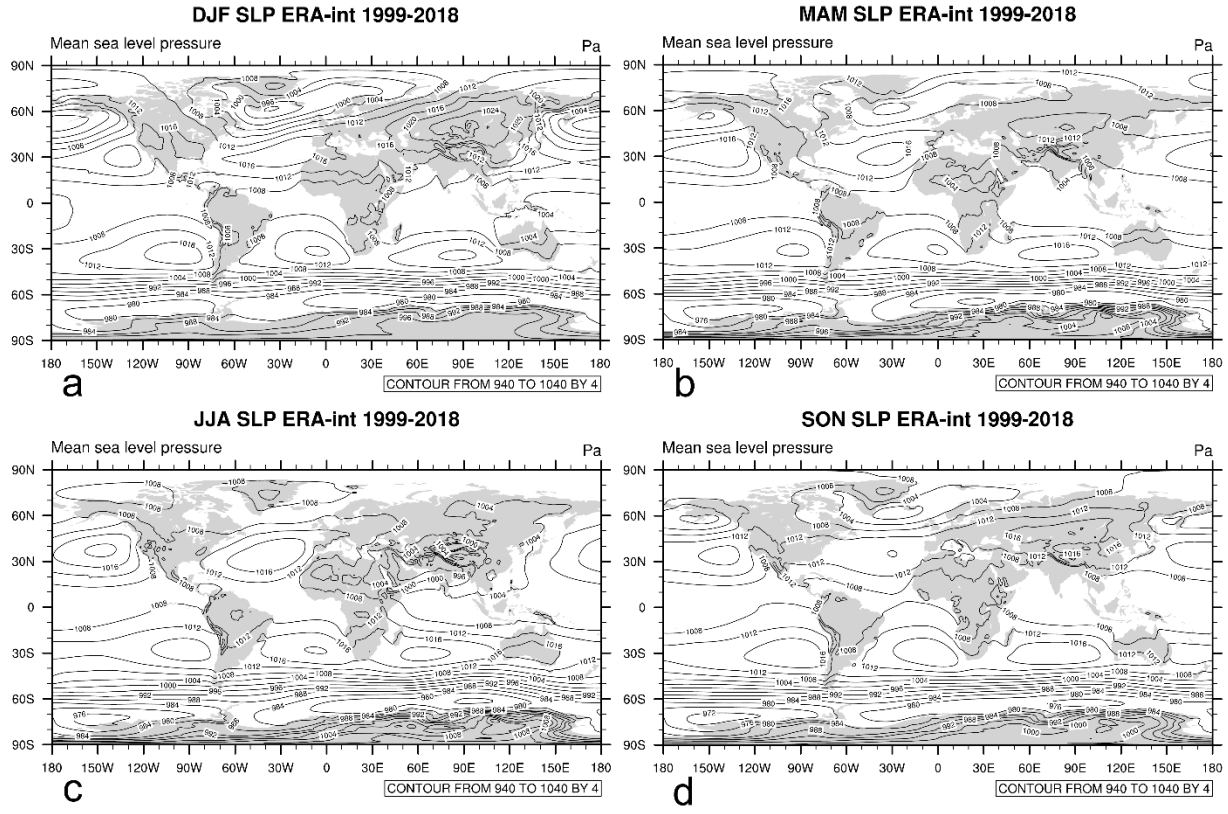

Figure 4.4 Time mean SLP contours in the four indicated extreme seasons (a) December–February, (b) March-May, (c) June–August, and (d) September-November. Contours use 4 hPa interval. European Centre for Medium-Range Weather Forecasts ERA-Interim Reanalysis data averaged from 1999 to 2018. Units are in hPa.

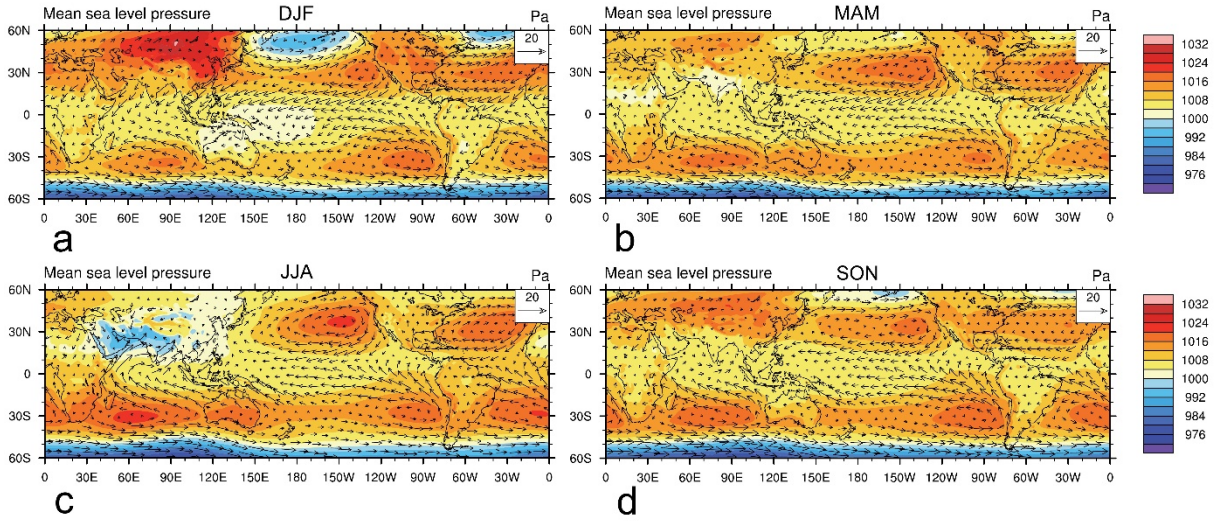

Figure 4.5. Time mean SLP contours paired with near surface (950 hPa) wind vectors. Panels use the corresponding seasons and data period as panels in Figure 4.4. The equatorial side of each subtropical SLP high provides the PGF to drive winds consistent with the lower branch of the "Hadley cell"; since those highs vary with longitude, so does the 'local' strength of the Hadley cell.

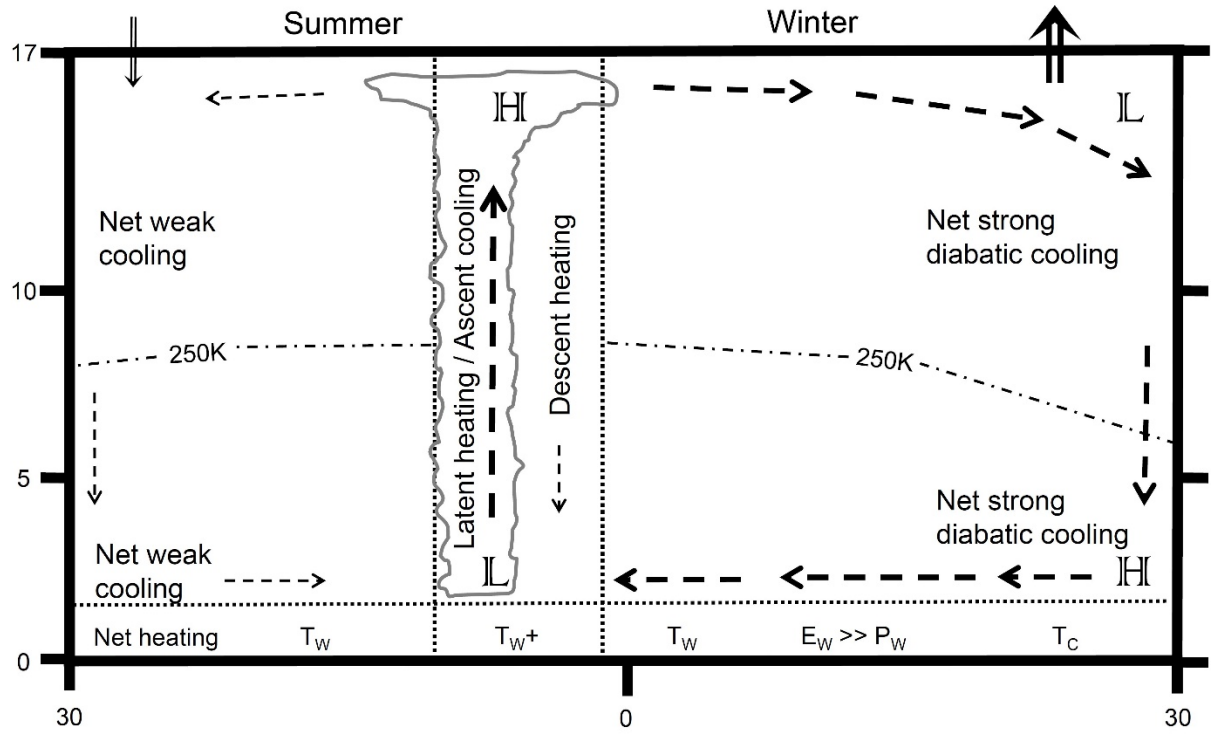

Figure 4.6 Schematic illustration of key elements of the Hadley circulation. The Hadley cell is stronger in the winter hemisphere due to greater radiative cooling in the winter subtropics, the latent heating by thunderstorms (whose areal extent is exaggerated greatly) is expressed in local sinking creating higher pressure aloft. The resultant upper level PGF drives the upper, poleward branch of the Hadley cell. Not only is the rising branch of the Hadley cell contained within tropical thunderstorms, this branch is the small amount of rising motion within the tropical thunderstorms that is not matched by adjacent, local sinking. Arrows at the top show TOA net radiation based on Figure 3.12; in the winter hemisphere there is strong net cooling at the poleward side of the subtropics; in the summer hemisphere there is weak net heating. The dot-dashed contour of T=250K is based on Figure 3.20 and intended to be representative of how the zonal mean temperature varies with latitude and thus, from the hypsometric relation, how the upper level pressure gradient varies. High and low pressure markers (H and L) are based on Figure 4.1. Thickness of the dashed line arrows intended to very roughly indicate the motion strength, using Figure 4.5 as well as data presented later. Surface temperatures ($T_W >> T_C$, with + sign to indicate slightly larger value). Heating information based on Trenberth and Smith (2008). Evaporation greatly exceeds precipitation in the winter subtropics ($E_W >> P_W$)

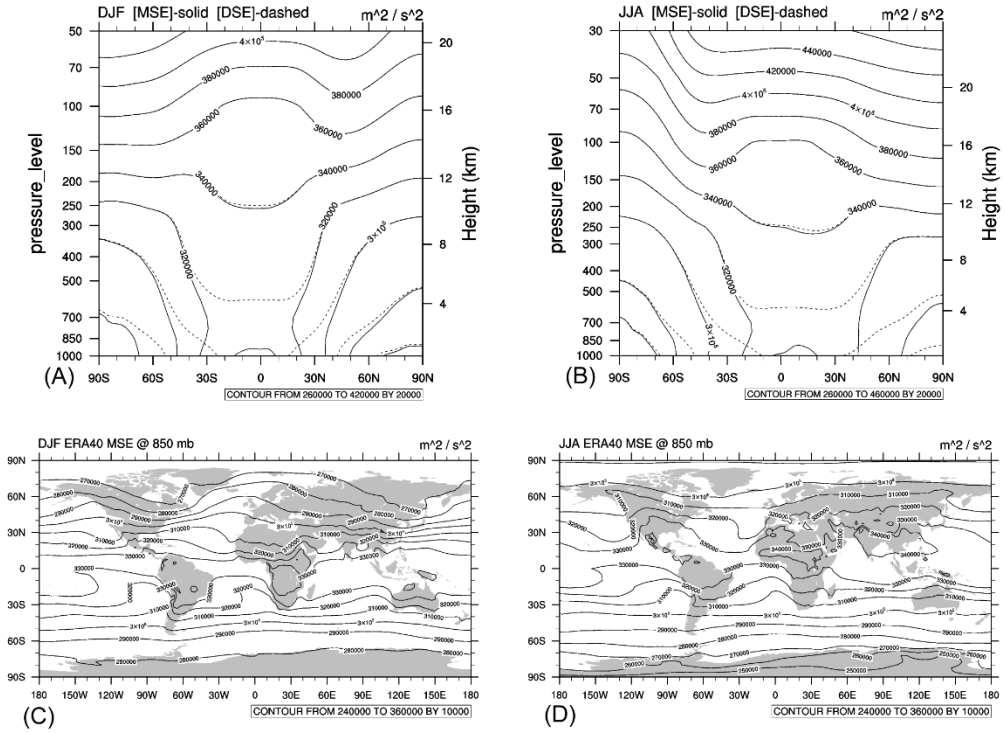

Figure 4.7 (a) DJF and (b) JJA zonal and seasonal average MSE. Contour interval of $2x10^4$ m^2s^{-2}. (c) DJF and (d) JJA seasonal average MSE at 850 hPa with contour interval of $1x10^4$ m^2s^{-2}. Figure panels reproduced from Grotjahn (2015b) using ERA-40 data from 1979-2001.

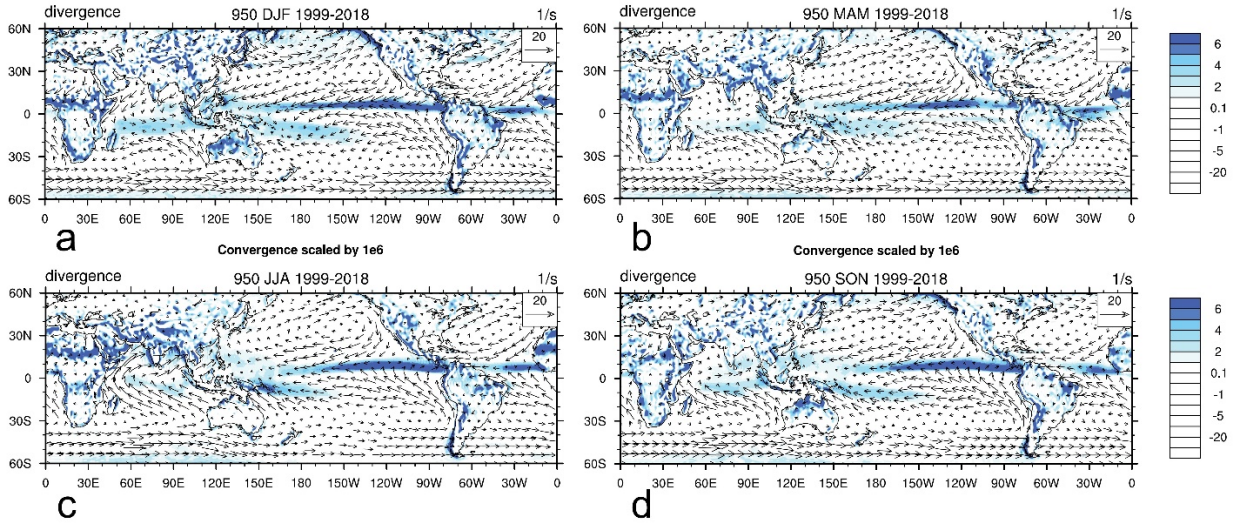

Figure 4.8. Near-surface horizontal flow at 950 hPa. The vectors compare with Figure 4.5. Regions of convergence are depicted as positive values with shading for values $>2x10^{-6}$ s^{-1}. The ICZ is generally apparent in low latitudes for convergence $>5x10^{-6}$ s^{-1}. (Other areas of strong convergence are created by topography and where there is persistent onshore flow at continental coasts.) Seasonal migration of the ICZ varies, being small in the eastern Pacific and large over land areas and Indian Ocean longitudes. Other convergent zones, like the South Pacific Convergence Zone (SPCZ) are evident in the western tropical Pacific, south of the equator. These months are not precise seasonal sobriquets; MAM and SON have some differences, notably over Southern Asia across Australia. ERA-Interim data from 1999-2018.

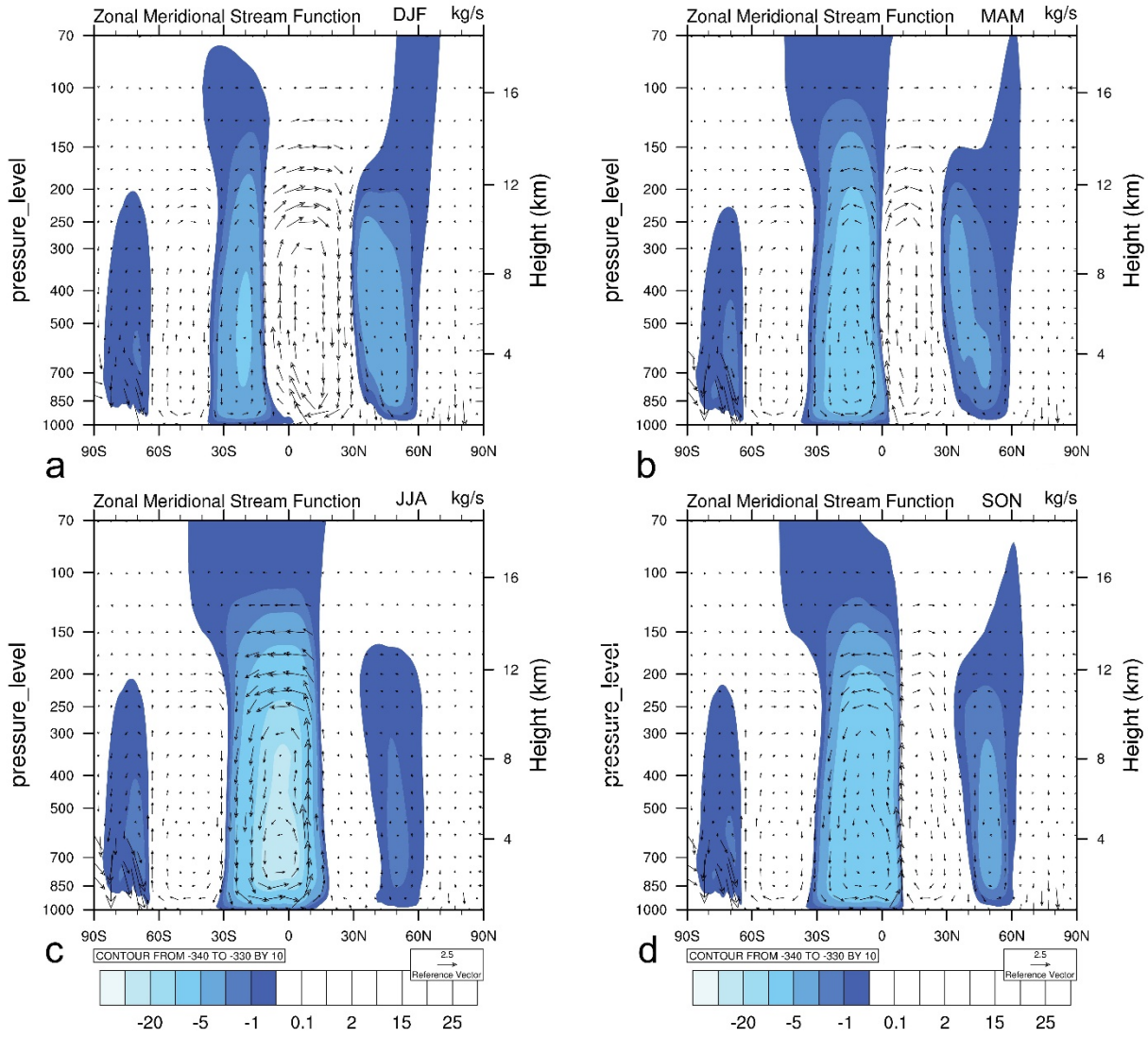

Figure 4.9. Meridional and pressure velocity vectors from zonal and seasonal averages of ERA-Interim data during 1999-2018. The corresponding stream function is contoured using shading for negative values (counter-clockwise circulation in this reference frame); the contours use a variable interval. The SHem 'Hadley' cell, the NHem 'Ferrel' cell, and the Antarctica circulation are shaded. The near equator, low-level convergence in Figure 4.8 may be compared with this figure. The dominance of the winter over the summer hemisphere Hadley circulations gives way to nearly-equal circulations in the transition seasons, MAM and SON.

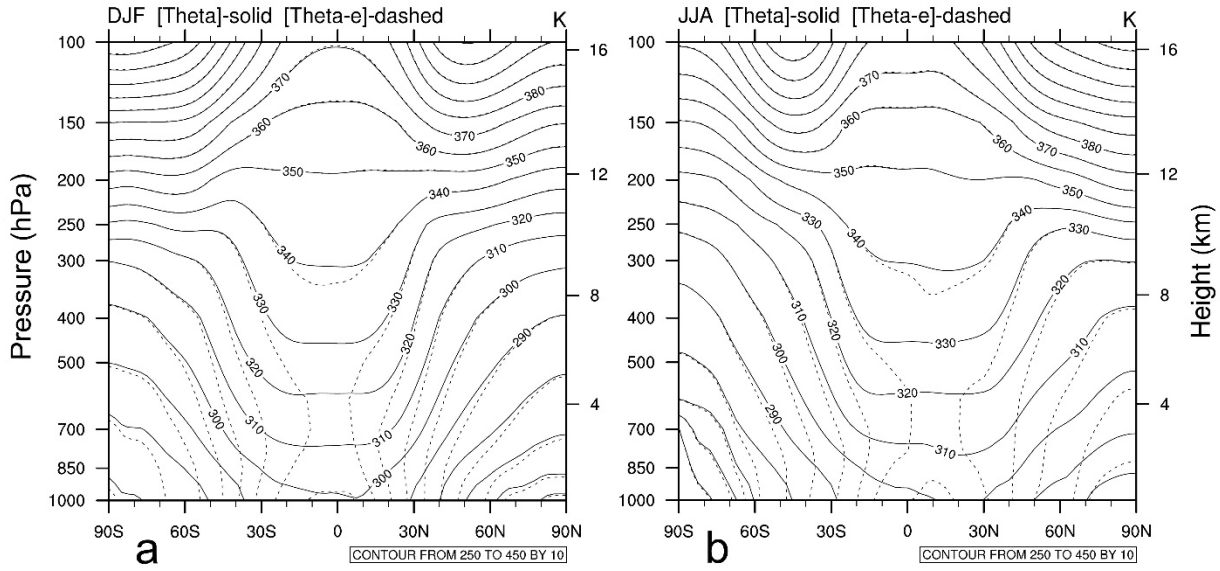

Figure 4.10. Meridional cross sections of [θ] (solid lines) and [θ_e] (dashed lines) for a) DJF and b) JJA averaged from 1979-2002 (ERA-40 data).

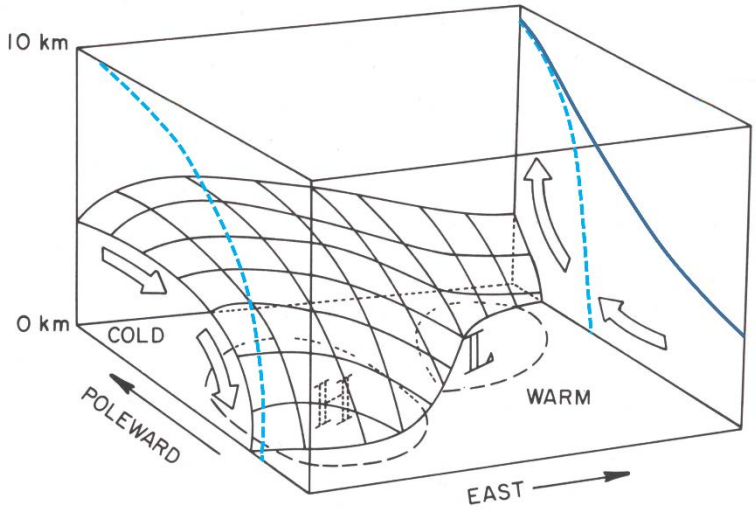

Figure 4.11. Schematic figure adapted from Grotjahn (1993; figure 3.18). Perspective view of an isentropic surface for a developing frontal cyclone to aid interpretation of Figure 4.12. Dashed lines on the box bottom are SLP contours with high (H) and low (L) centers marked. Large arrows indicate some representative air motions relative to this frontal cyclone. When projected onto the east face, these arrows look like the Ferrel cell. However, relative to the θ surface, the warm sector arrows are at higher θ than the cold sector arrows, and motion in isentropic coordinates looks thermally-direct. The dotted lines indicate where a representative θ_e surface might intersect the east and west faces of the box. The solid line on the east face is where the θ equals that θ_e value at that longitude.

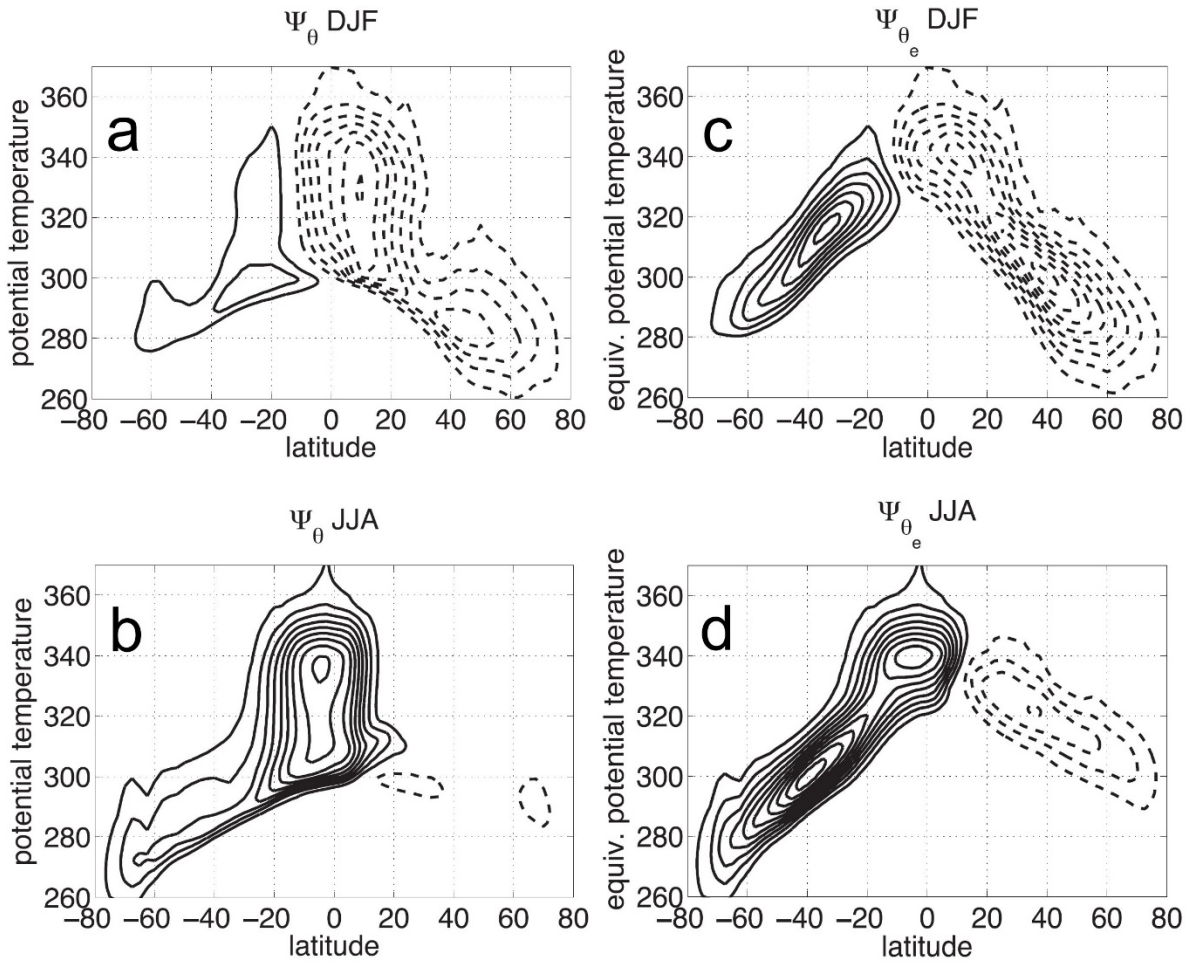

Figure 4.12. Time and zonal mean stream function where dashed lines indicate clockwise motion and solid lines counter clockwise motion in the meridional plane. Stream function in isentropic vertical coordinate a) DJF and b) JJA. Stream function in equivalent potential temperature coordinate deduced from a statistical extension of the TEM system c) DJF and d) JJA. Figures adapted from Pauluis et al. (2011).

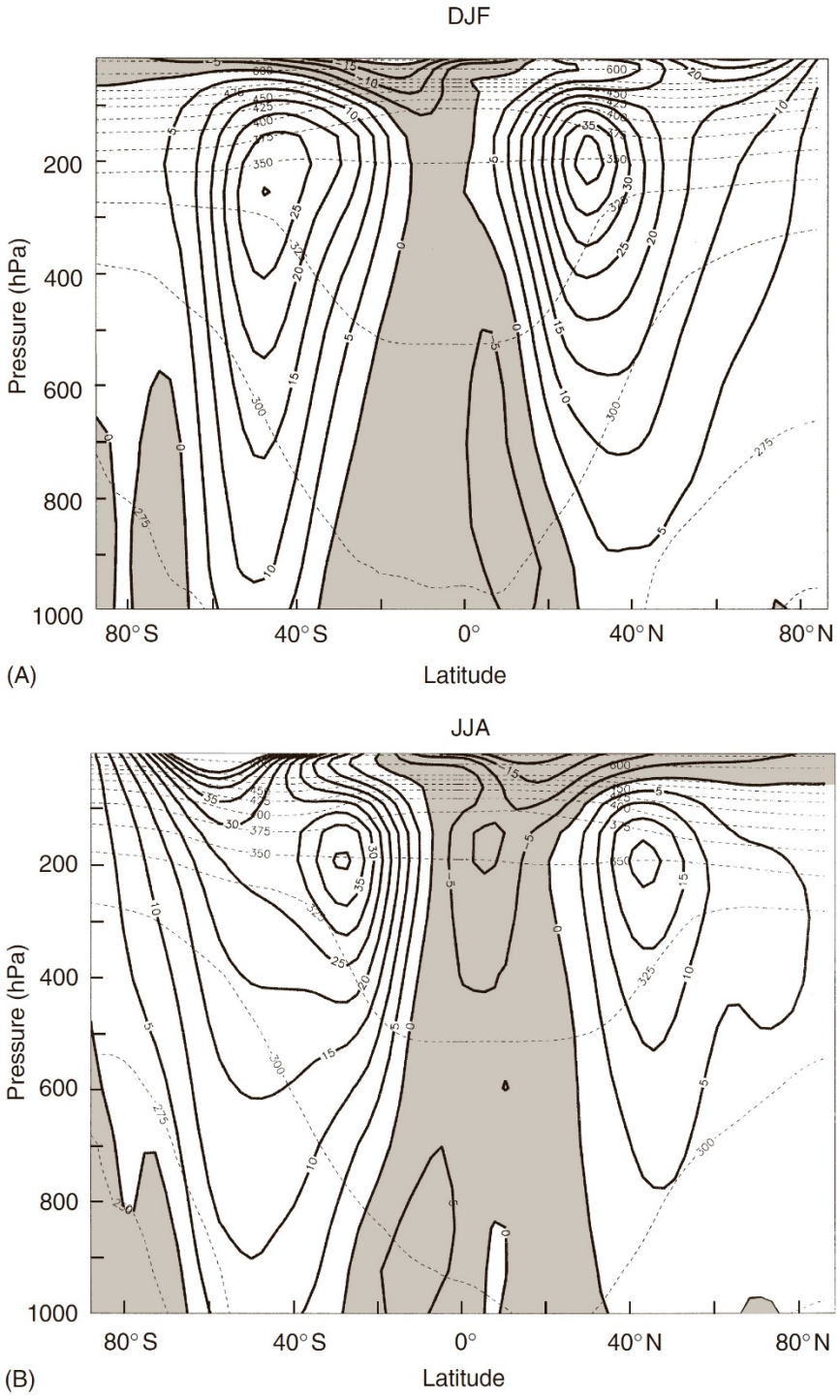

Figure 4.13. Zonal and seasonal average zonal wind (solid contours), negative values, i.e. easterly winds are shaded. Corresponding average potential temperature (dashed contours) also shown to illustrate thermal wind shear. The contour intervals are 5 m/s and 25 K. Contours >50m/s in the SHem polar night jet are not drawn NCEP/NCAR reanalysis data from 1979-1999 shown. Figure reproduced from Grotjahn (2015a).

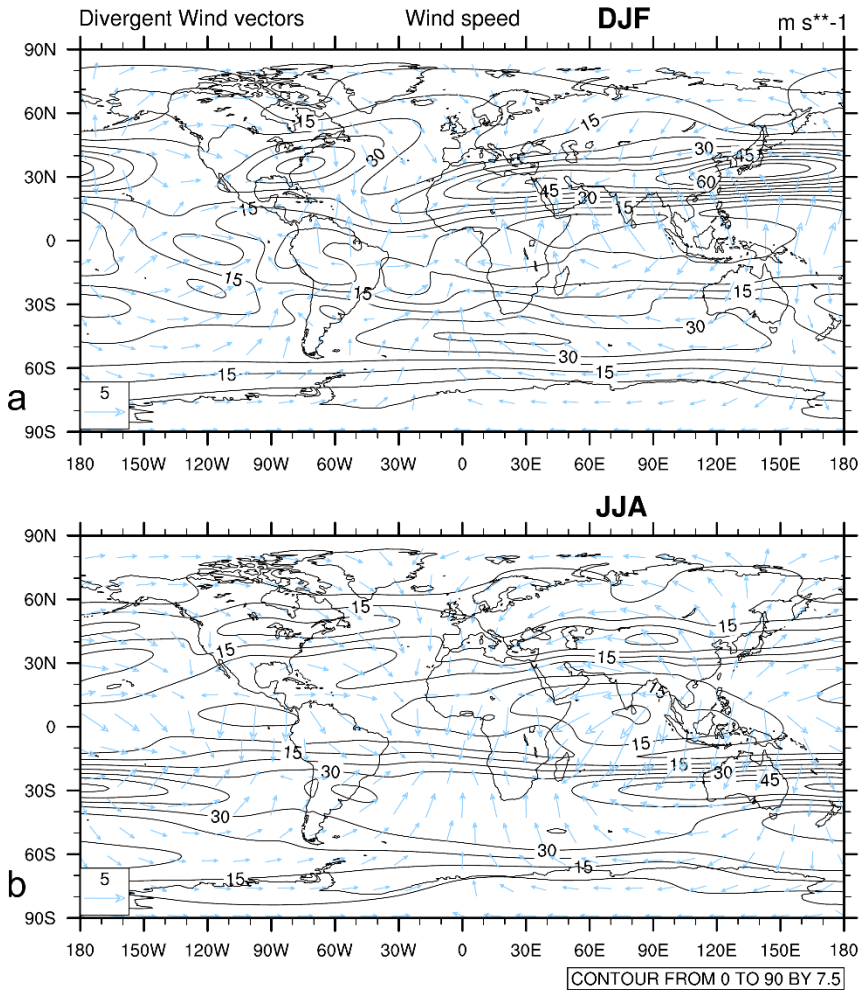

Figure 4.14. (a) DJF and (b) JJA seasonal averages of winds at 200 hPa. Specifically: wind speed (contoured, 5 m/s interval) and divergent winds (vectors, scale inset at lower left). The subtropical jet streams of Figure 4.13 have relative maxima, often near the east coasts of continents (consistent with stationary, planetary wave troughs). The contour encircling Sri Lanka during JJA is 22.5m/s due to an easterly jet. Though these divergent winds imperfectly approximate ageostrophic winds, the divergent winds tend to have a poleward component where westerly winds are accelerating (and *vice versa*) in the subtropical jet streams. ERA-Interim data from 1999-2018 shown.

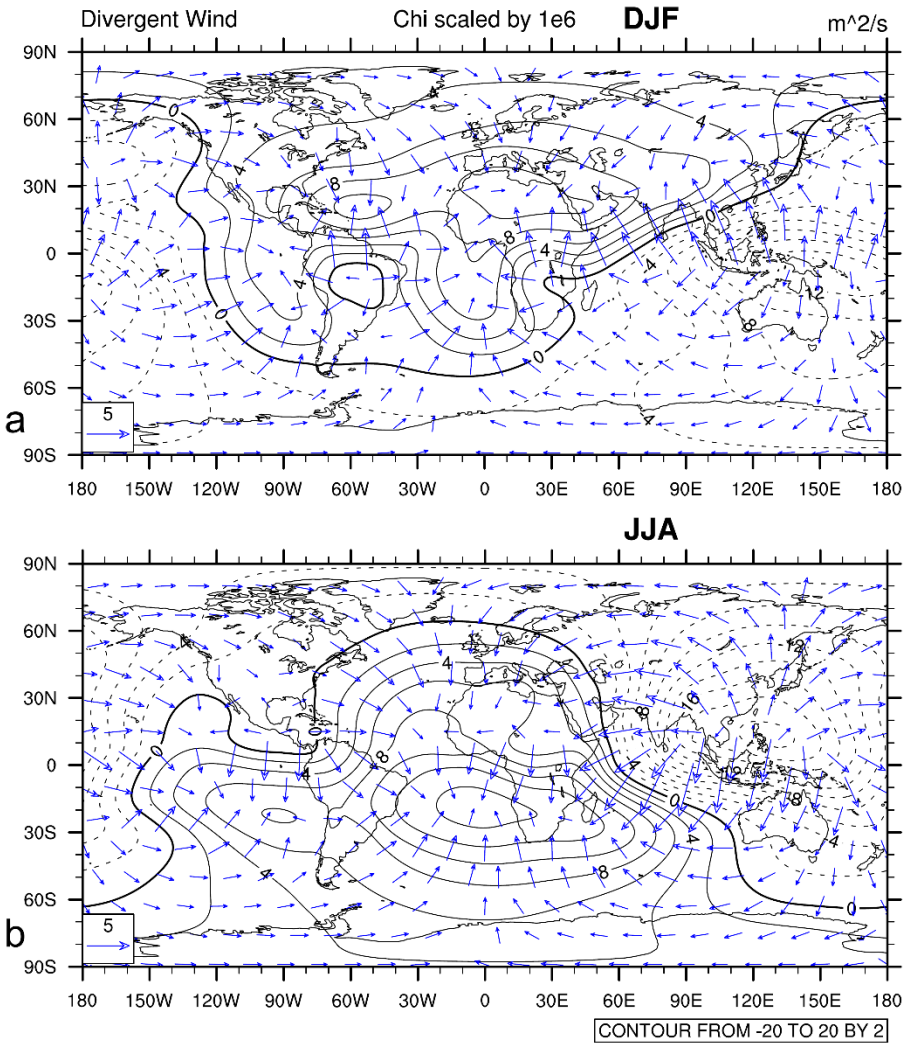

Figure 4.15. Similar to Figure 4.14 except the contours are of velocity potential, also at 200 hPa. By definition, divergent flow radiates from negative centers and while flow into positive centers is convergent. In addition to flow consistent with the winter 'Hadley' cell there is notable east-west flow, such as the 'Walker' circulation across the Pacific.

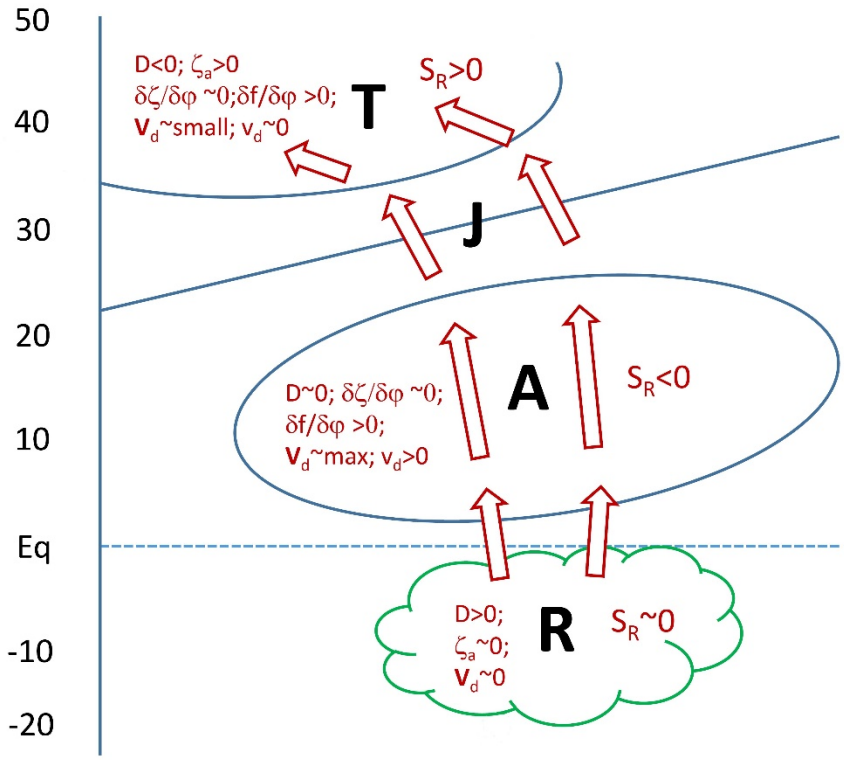

Figure 4.16. Schematic diagram of how a region of tropical convection (green 'cloud' labeled R) to a midlatitude trough (indicated by solid contours of stream function Ψ values) is linked with strong upper level convergence (labeled T) via divergent winds. The equator is marked by a dotted line. The Rossby wave source, S_R at tropopause level (to neglect vertical motion terms) creates an anticyclone (labeled A) that is offset from the convection and which amplifies the height gradient and thus the subtropical jet (labeled J).

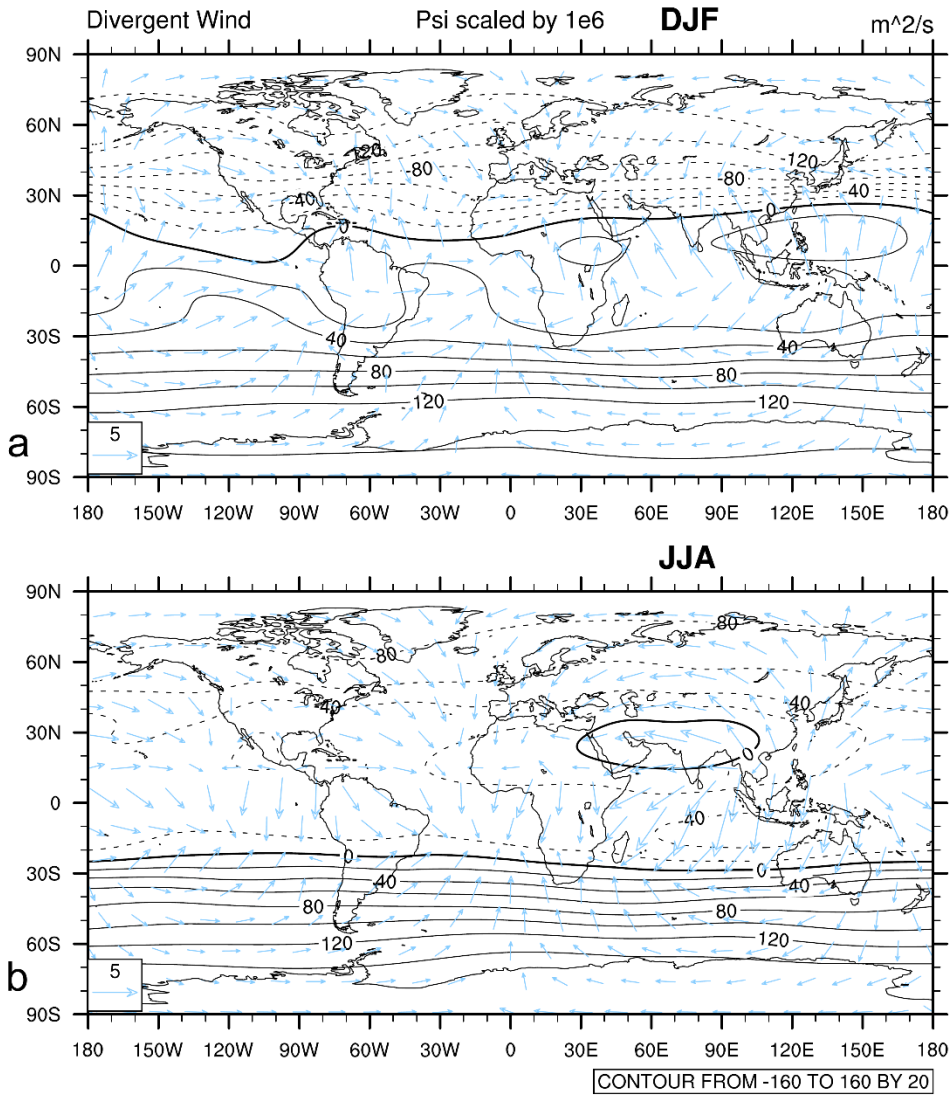

Figure 4.17. Similar to Figure 4.14 except the contours are of stream function, Ψ also at 200 hPa. Considering Figures 4.14-4.17 together, the circulation elements over the tropical western Pacific to eastern Asia during DJF are similar to the schematic Figure 4.16. During JJA, southeast Asian monsoon convection creates a SHem anticyclone (-40 contour) that enhances the Ψ gradient over Australia and the subtropical jet there.

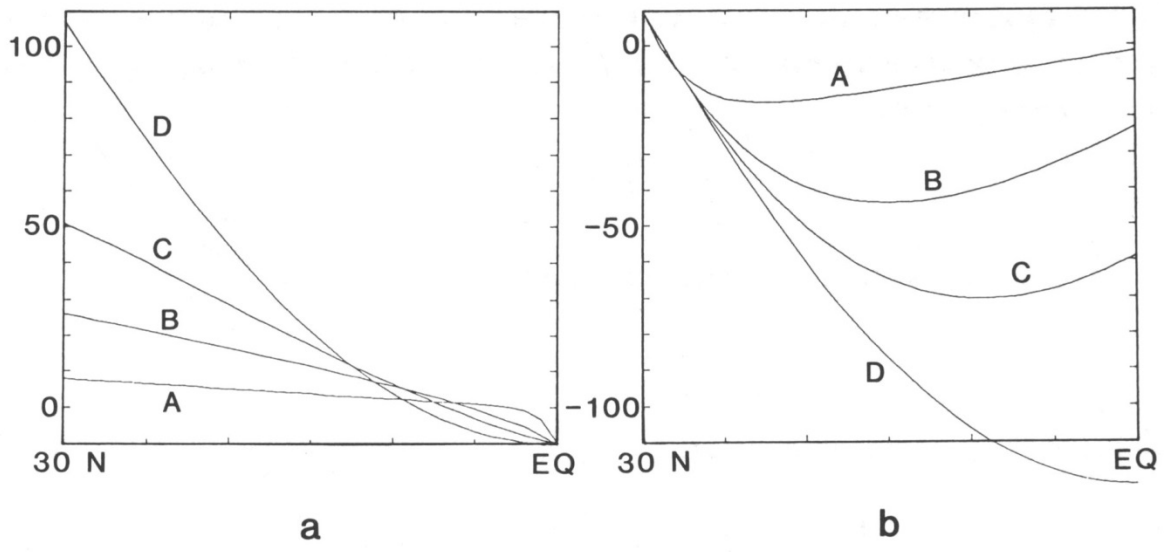

Figure 4.18. Example solutions for various magnitudes of the meridional velocity. (a) Solutions for poleward motion: [v] equals 5 mm/s (curve A), 2 cm/s (curve B), 5 cm/s (curve C) and no viscosity (curve D). The viscous solutions use $k_{Rf} = -4.82 \times 10^{-8}$ s^{-1}. (b) Solutions for equatorward motion: [v] equals 50 cm/s (curve A), 2 m/s (curve B), 5 m/s (curve C) and no viscosity (curve D). The viscous solutions use $k_{Rb} = -1.8 \times 10^{-6}$ s^{-1}.

Homework ideas.

1. Est. the tropical easterly jet from M cons. Over India
2. Estimate SLP change for ave T drop of X in 100 hPa bndry layer above sfc.
3. Hadley cell: evaluate 500-200 hPa thickness at 30N and equator zonal ave. See Troup (1965) for Walker Circ. application of same idea p.11-422. in R book.
4. merid HF by mean meridional cells (partial cancellation) Net Heat flux estimate for the Hadley cell?

5. Compare zonal average meridional T gradient when fronts are both intensified and displaced in a wavy pattern. Compare with real data?

HWK-or-topic:

Combine U, V, and T gradient with thermal wind and friction: Create diagrams that show the balance between meridional motion V – ang momentum increases U – transports heat that reduces meridional T gradient and hence vertical shear of U – and friction. For example, a schematic line with V in the horizontal against different vertical axes of values at a specific latitude, say, 38N: U from M cons. with solid (flat?) for U frictionless values and dashed for strong friction, dT/dy decreasing as V increases, U from dU/dz thermal wind (again using solid line; unclear how friction would enter)

1. Radiative cooling rate as a function of elevation for a lapse rate that varies with pressure and latitude? – CHAPTER 3???

2. Scale analysis similar to Charney 1963?

5. {{For figure 4.11: Think of how the vertical shear may increase locally (by intensifying a frontal zone temperature gradient) while at the same time air masses are displaced. So, the zonal average temperature gradient seems reduced. (This could probably be shown with a hwk problem.)

6. Calculate estimates of sensible and latent heat flux in JJA and DJF using the values of DSE and MSE-DSE along with estimated [v] values at specific latitudes. Then compare with figures in Chapter 3? But we don't have the vertical average LHF! Need to find a reference and maybe put add a fig to chapter 3 or include that figure in this problem section.

7. Derive the spherical coordinates form of the [u] tendency equation (4.23).

New References

Johnson, D.R. 1989: The forcing and maintenance of global monsoonal circulations: an isentropic analysis. Adv. In Geophysics, 31, 43-329.

Chapter references:

Richard Grotjahn* and Muhtarjan Osman 2006 Remote weather associated with North Pacific subtropical sea-level high properties NTERNATIONAL JOURNAL OF CLIMATOLOGY Int. J. Climatol. 27: 587–602 (2007) Published online 12 October in Wiley InterScience (www.interscience.wiley.com) DOI: 10.1002/joc.1423

van Loon (1966) On the annual temperature range over the Southern Oceans. Geographical Review 56: 497–515.

Whitaker and Horn (1984) Northern Hemisphere extratropical cyclone activity for four mid-season months. Journal of Climatology 4: 297–310.

Simmonds and Murray (1999) Southern extratropical cyclone behavior in ECMWF analyses during the FROST special observing periods. Weather and Forecasting 14: 878–891.

Hoskins and Hodges (2002) New perspectives on the Northern Hemisphere winter storm tracks. Journal of the Atmospheric Sciences 59: 1041–1061.

Hoskins and Hodges (2005) A new perspective on Southern Hemisphere storm tracks. Journal of Climate 18: 4108–4129.

MDS Mesquita NG Kvamstø, A Sorteberg & D E. Atkinson (2008) Climatological properties of summertime extra-tropical storm tracks in the Northern Hemisphere. Tellus 60A: 557–569. DOI: 10.1111/j.1600-0870.2007.00305.x